TU Delft

Delft University of Technology

Combined Large-Eddy and Direct Numerical Simulations of a Planar Jet with Heated Co-Flow with Medium and Low Prandtl Fluids

Cascioli, E.; Keijers, S.; Van Tichelen, K.; Vesper, J. E.; Kenjeres, S.

DOI
10.1016/j.ijheatmasstransfer.2022.122774

Publication date
2022

Document Version
Final published version

Published in
International Journal of Heat and Mass Transfer

Citation (APA)
Cascioli, E., Keijers, S., Van Tichelen, K., Vesper, J. E., & Kenjeres, S. (2022). Combined Large-Eddy and Direct Numerical Simulations of a Planar Jet with Heated Co-Flow with Medium and Low Prandtl Fluids. *International Journal of Heat and Mass Transfer*, *191*, Article 122774. https://doi.org/10.1016/j.ijheatmasstransfer.2022.122774

Important note
To cite this publication, please use the final published version (if applicable).
Please check the document version above.

Copyright
Other than for strictly personal use, it is not permitted to download, forward or distribute the text or part of it, without the consent of the author(s) and/or copyright holder(s), unless the work is under an open content license such as Creative Commons.

Takedown policy
Please contact us and provide details if you believe this document breaches copyrights.
We will remove access to the work immediately and investigate your claim.

This work is downloaded from Delft University of Technology.
For technical reasons the number of authors shown on this cover page is limited to a maximum of 10.

International Journal of Heat and Mass Transfer 191 (2022) 122774

Contents lists available at ScienceDirect

International Journal of Heat and Mass Transfer

journal homepage: www.elsevier.com/locate/hmt

Combined Large-Eddy and Direct Numerical Simulations of a Planar Jet with Heated Co-Flow with Medium and Low Prandtl Fluids

E. Cascioli[a,b], S. Keijers[b], K. Van Tichelen[b], J.E. Vesper[a], S. Kenjereš[a,*]

[a] Delft University of Technology, Faculty of Applied Sciences, Department of Chemical Engineering and J. M. Burgerscentrum Research School for Fluid Mechanics, Van der Maasweg 9, Delft 2629 HZ, The Netherlands
[b] SCK.CEN, Belgian Nuclear Research Centre, Boeretang 200, Mol 2400, Belgium

ARTICLE INFO

Article history:
Received 12 July 2021
Revised 24 February 2022
Accepted 6 March 2022
Available online 26 March 2022

Keywords:
Large-eddy simulation
Planar jet
Forced convection
Low-Prandtl fluids

ABSTRACT

In the present work, we have applied a combined dynamic large-eddy simulation (LES) and direct numerical simulation (DNS) approach for a three-dimensional planar jet in a turbulent forced convection regime (Re = 18000) with a heated co-flow. Results from LES are compared with Reynolds Averaged Navier-Stokes (RANS) simulations and experimental data. We have analyzed flow and heat transfer features for four values of the characteristic Prandtl numbers (Pr = 0.71, 0.2, 0.025, and 0.006), which are representatives of air, He-Xe gas mixture, Lead-Bismuth Eutectic (LBE), and sodium, respectively. The latter two low-Prandtl fluids have been considered because of their role as primary coolants in advanced fast pool-type reactor prototypes (such as the Multi-purpose Hybrid Research Reactor for High-tech Applications (MYRRHA) at SCK•CEN, Belgium). We have provided detailed insights into instantaneous and long-term time-averaged behavior of the velocity and temperature fields (the first- and second-order moments). Furthermore, we have analyzed profiles of characteristic velocity and temperature time scales and dissipation rates, as well as the power spectra of the streamwise velocity component and temperature at several characteristic locations. The mean temperature profiles demonstrated rather low sensitivity for various values of the Prandtl number. In contrast, profiles of the temperature standard deviation exhibited larger variations, decreasing in magnitude with lower Prandtl values. Here presented results of the high fidelity numerical simulations (dynamic LES/DNS) for the low-Prandtl working fluids can be used for further development, testing, and validation of the advanced RANS-type turbulence models.

© 2022 The Author(s). Published by Elsevier Ltd.
This is an open access article under the CC BY license (http://creativecommons.org/licenses/by/4.0/)

1. Introduction

Computational Fluid Dynamics (CFD) represents a powerful tool for thermal-hydraulics investigations, supporting both the design phase and safety analyses of advanced nuclear reactors. The **M**ulti-purpose H**y**brid **R**esearch **R**eactor for **H**igh-tech **A**pplications (MYRRHA) is a prototype of advanced nuclear reactor technology cooled by liquid LBE, which is under design at the Belgian Nuclear Research Centre (SCK•CEN) [1]. This nuclear reactor prototype is characterized by a pool-type configuration in which all primary components are contained inside the main vessel. In this study, we focused on the upper and lower plena, where the jet-like mixing phenomena take place, [2]. Standard CFD tools are based on the Reynolds Averaged Navier-Stokes (RANS) approach where the eddy-diffusivity and a simple-gradient hypothesis are used as models of the turbulent momentum and heat flux, respectively, [3]. Furthermore, by introducing a constant turbulent Prandtl number (a ratio between eddy viscosity and eddy diffusivity), the Reynolds analogy is usually assumed between the dynamics of the turbulent velocity and thermal fields, [4]. This simplified approach demonstrated relatively good performances and reliability for working fluids with Prandtl number values close to the one (i.e. $Pr \approx 1$). For the low-Prandtl number fluids, such as liquid metals, this simplified approach does not hold and more advanced turbulent heat transfer (THT) models are required, [5]. Suitable options for industrial applications are four-equations ($k-\epsilon-k_\theta-\varepsilon_\theta$) models in combination with algebraic turbulent heat flux (AFM) models, [6], [7–10]. Due to the complexity of such RANS-type of turbulence models, there is a continuous need for their detailed validation in various flow configurations and over a wide range of working parameters.

* Corresponding author.
E-mail address: s.kenjeres@tudelft.nl (S. Kenjereš).

https://doi.org/10.1016/j.ijheatmasstransfer.2022.122774
0017-9310/© 2022 The Author(s). Published by Elsevier Ltd. This is an open access article under the CC BY license (http://creativecommons.org/licenses/by/4.0/)

The detailed flow field characteristics and theoretical behavior of a turbulent submerged jet impingement were addressed in [13]. Transient features of the rectangular jet at a relatively low value of Reynolds number (Re = 2000) were presented in [14]. Numerical validation of the four-equation RANS-type of turbulence model for the impinging jet test case was performed in [10]. The high-fidelity LES and DNS studies were performed for low-Prandtl fluids in the backward-facing step ([11]) and natural convection boundary layer ([12]), respectively.

The experimental investigations of the low-Prandtl fluids are challenging due to numerous limitations of measuring techniques, especially when the turbulent heat transfer is of main interest. Some important experimental studies of turbulent single jet flow for Pr < 1 fluids were conducted at the Karlsruhe Institute of Technology (KIT) ([15]), and more recently at the von Karman Institute for Fluid Dynamics (VKI) ([16]). In the former, a confined heated sodium jet was analyzed in forced-, mixed-, and natural-convection regimes. In the latter, the MYRTE wind tunnel investigations were performed of a cold forced-convection planar jet surrounded by heated co-flows with air (Pr = 0.71) and He-Xe gas mixture (Pr = 0.2) as working fluids.

In the present work, we perform the combined dynamic LES and DNS simulations of a simplified setup of the MYRTE wind tunnel, which was previously discussed and studied by using RANS-based turbulence model simulations, [18]. We cover an extensive range of Prandtl numbers: for air (Pr = 0.71), He-Xe gas mixture (Pr = 0.2) (operative working fluids of the MYRTE wind tunnel), as well as for liquid metals, Lead-Bismuth Eutectic (LBE, which is the primary coolant of the MYRRHA nuclear reactor) (Pr = 0.025) and sodium (Pr = 0.006). We present the first- and second-order statistics of the velocity and temperature fields, as well as characteristic mechanical and thermal time-scales. Frequency-based power spectra of velocity and temperature at characteristic locations are analyzed too. This database can be used for additional validation and testing of advanced RANS models for forced-convection flows of low-Prandtl fluids, complementing the recent numerical studies of [19]. The possible future extensions include the application of such validated models for simulations of the complex multiple-jets in mixed ([20]) and natural convection regimes ([21]).

2. Numerical Method

2.1. Fundamental equations

The fundamental transport equations of the instantaneous velocity and a passive scalar (temperature) are the conservation of mass, momentum and energy, as follows:

$$\frac{\partial \hat{U}_i}{\partial x_i} = 0 \tag{1}$$

$$\frac{\partial \hat{U}_i}{\partial t} + \frac{\partial \hat{U}_i \hat{U}_j}{\partial x_j} = -\frac{1}{\rho}\frac{\partial \hat{p}}{\partial x_i} + \nu \frac{\partial^2 \hat{U}_i}{\partial {x_j}^2} \tag{2}$$

$$\frac{\partial \hat{T}}{\partial t} + \frac{\partial \hat{U}_j \hat{T}}{\partial x_j} = \alpha \frac{\partial^2 \hat{T}}{\partial {x_j}^2} \tag{3}$$

where ρ, ν and α are the molecular density, kinematic viscosity and thermal diffusivity, respectively. In the present study, all thermophysical fluid properties are assumed to be constant. In the LES technique, a filtering operation is applied to instantaneous variables as:

$$\bar{f}(x) = \int_D \hat{f}(x') G(x, x', \bar{\Delta}) dx' \tag{4}$$

where D is the entire domain and G is the filter function. The latter determines the smallest size of turbulent and thermal structures which can be directly resolved. This size is related to the filter width, $\bar{\Delta}$. In most cases, the filter width is taken to be proportional to the grid cell length, l_c, as $\bar{\Delta} = n\ l_c$. In this work, $n = 1$ and for this reason unfiltered structures will be directly addressed as SubGrid-Scales (SGS). Applying Eq. 4 to Eqs. 2 and 3, filtered quantities (denoted with '-') appear in transport equations as:

$$\frac{\partial \overline{U_i}}{\partial t} + \frac{\partial \overline{U_i}\ \overline{U_j}}{\partial x_j} = -\frac{1}{\rho}\frac{\partial \overline{p}}{\partial x_i} - \frac{\partial \tau_{ij}}{\partial x_j} + \nu \frac{\partial^2 \overline{U_i}}{\partial {x_j}^2} \tag{5}$$

$$\frac{\partial \overline{T}}{\partial t} + \frac{\partial \overline{U_j}\ \overline{T}}{\partial x_j} = -\frac{\partial q_j}{\partial x_j} + \alpha \frac{\partial^2 \overline{T}}{\partial {x_j}^2} \tag{6}$$

where the SGS turbulent stresses, τ_{ij}, and turbulent heat flux, q_j, can be also defined as:

$$\tau_{ij} = \overline{U_i U_j} - \overline{U_i}\ \overline{U_j} \tag{7}$$

$$q_j = \overline{U_j T} - \overline{U_j}\ \overline{T} \tag{8}$$

and need to be modeled, [3].

2.2. Dynamic subgrid-scale Smagorinsky model

The dynamic estimate of the SGS contributions ([22]) significantly improved performances of the standard Smagorinsky approach, [23]. In the dynamic procedure, the SGS model coefficients are not prescribed *a priori*, but are locally calculated during the LES runtime. This is achieved by defining a test grid (denoted with '~'), whose width is $\tilde{\bar{\Delta}} = 2\bar{\Delta}$. Then, by applying the test-filter over the momentum equation, a new subtest-stress tensor (T_{ij}) is obtained as

$$T_{ij} = \widetilde{\overline{U_i U_j}} - \tilde{\overline{U_i}}\ \tilde{\overline{U_j}} \tag{9}$$

It is shown in [22] that resolved stress can be expressed as

$$L_{ij} = T_{ij} - \widetilde{\tau_{ij}} \tag{10}$$

and it can be explicitly evaluated from the large-scales as

$$L_{ij} = \widetilde{\overline{U_i}\ \overline{U_j}} - \tilde{\overline{U_i}}\ \tilde{\overline{U_j}} \tag{11}$$

The same closure Smagorinsky model is applied for both the grid-filter and test-filter turbulent stress with an identical value of the model coefficient C_s, and it can be written as:

$$\tau_{ij} - \frac{1}{3}\delta_{ij}\tau_{kk} = -2C_s\overline{\bar{\Delta}^2}|\overline{\bar{S}}|\overline{\bar{S}_{ij}} \tag{12}$$

$$T_{ij} - \frac{1}{3}\delta_{ij}T_{kk} = -2C_s\tilde{\bar{\Delta}}^2|\tilde{\bar{S}}|\tilde{\bar{S}}_{ij} \tag{13}$$

where C_s is the dynamic Smagorinsky constant (to be determined), $\overline{\bar{S}_{ij}} = \frac{1}{2}\left(\frac{\partial \overline{U_i}}{\partial x_j} + \frac{\partial \overline{U_j}}{\partial x_i}\right)$ and $\tilde{\bar{S}}_{ij} = \frac{1}{2}\left(\frac{\partial \tilde{\overline{U_i}}}{\partial x_j} + \frac{\partial \tilde{\overline{U_j}}}{\partial x_i}\right)$ are the strain rate tensors evaluated at the grid-filter $\bar{\Delta}$ and test-filter $\tilde{\bar{\Delta}}$, respectively. By combining Eqs. (10), (12) and (13), we have:

$$L_{ij} - \frac{1}{3}\delta_{ij}L_{kk} = 2C_s M_{ij} \tag{14}$$

where

$$M_{ij} = \tilde{\bar{\Delta}}^2|\tilde{\bar{S}}|\tilde{\bar{S}}_{ij} - \overline{\bar{\Delta}^2|\bar{S}|\bar{S}_{ij}} \tag{15}$$

An adaptation of the original [22] model was proposed in [24] who applied a least squares method to find an optimal value of C_s by minimizing the error in Eq. (14) as:

$$\left(e_{ij}\right)^2 = \left(L_{ij} - \frac{1}{3}\delta_{ij}L_{kk} - 2C_sM_{ij}\right)^2 \tag{16}$$

Since $e_{ij} = e_{ij}(C_s)$, by evaluating its first derivative in respect to C_s, i.e. $\partial\left(e_{ij}\right)^2/\partial C_s = 0$, we have

$$C_s = \frac{1}{2}\frac{L_{ij}M_{ij}}{M_{ij}^2} \tag{17}$$

Finally, the turbulent SGS viscosity is calculated as:

$$\nu_{SGS} = C_s\overline{\Delta}^2|\bar{S}| \tag{18}$$

which makes a complete closure of the filtered momentum equation. In the present work, instead of applying spatial averaging of C_s in the homogeneous directions, we introduce a local spatial averaging involving six neighboring control volumes. This local averaging procedure makes this approach suitable also for complex geometries. Furthermore, the SGS turbulent viscosity was also bounded such that $\nu_{SGS} \geq -\nu$, allowing for at least some backscattering, [25,26].

2.3. Dynamic subgrid-scale turbulent Prandtl model

A standard approach to model the thermal SGS is to use the Reynolds analogy through imposing the turbulent Prandtl number as a scaling coefficient ([27,28]):

$$\alpha_{SGS} = \frac{\nu_{SGS}}{\mathrm{Pr}_{SGS}} \tag{19}$$

Now, by imposing a simple-gradient-diffusion hypothesis (SGDH), the unresolved turbulent heat flux will be calculated as

$$q_j = -\alpha_{SGS}\frac{\partial\overline{T}}{\partial x_j} \tag{20}$$

In the present work, to make fully consistent dynamic procedure for both velocity and temperature fields, the turbulent Prandtl number is estimated similarly to the Smagorinsky coefficient presented above, [29]. Again, a least-square minimization is applied to obtain the smallest differences between the closure assumption and resolved turbulent heat flux ([30,31]) as:

$$\frac{1}{\mathrm{Pr}_{SGS}} = \frac{M_{ik}^2}{L_{ik}M_{ik}}\frac{P_jR_j}{P_j^2} \tag{21}$$

where:

$$L_{ik} = -\widetilde{\overline{U_i}\,\overline{U_k}} + \widetilde{\overline{U}_i}\,\widetilde{\overline{U}_k} \tag{22}$$

$$M_{ik} = \overline{\Delta}^2\,|\,\widetilde{\bar{S}}\,|\,\widetilde{\bar{S}_{ik}} - \overline{\Delta}^2\,\widetilde{|\,\bar{S}\,|\,\bar{S}_{ik}} \tag{23}$$

$$R_j = \widetilde{\overline{\Delta}}^2\,|\,\widetilde{\bar{S}}\,|\,\widetilde{\frac{\partial\overline{T}}{\partial x_j}} - \widetilde{\overline{\Delta}}^2\,\widetilde{|\,\bar{S}\,|\,\frac{\partial\overline{T}}{\partial x_j}} \tag{24}$$

The P_j is the test-filter resolved heat flux, which can be directly calculated from the resolved test-filter fields as:

$$P_j = \widetilde{\overline{U_j}\,\overline{T}} - \widetilde{\overline{U}_j}\,\widetilde{\overline{T}} \tag{25}$$

Finally, we also bounded the thermal SGS diffusivity similarly to the SGS viscosity such that $\alpha_{SGS} \geq -\alpha$.

2.4. Computational code

The OpenFOAM-2.4.0 CFD code is used to perform the dynamic large-eddy simulations. The dynamic SGS treatment for both momentum and temperature is originally implemented through additional source code libraries. The PISO algorithm is used for coupling between the velocity and pressure fields, [17]. The second-order central-differencing scheme (CDS) is used to discretize gradient, Laplacian, and divergence terms of transport equations. The second-order backward implicit scheme is applied for the time integration. The maximum local Courant number is limited to 1.2, whereas its mean value is kept below the 1, [32].

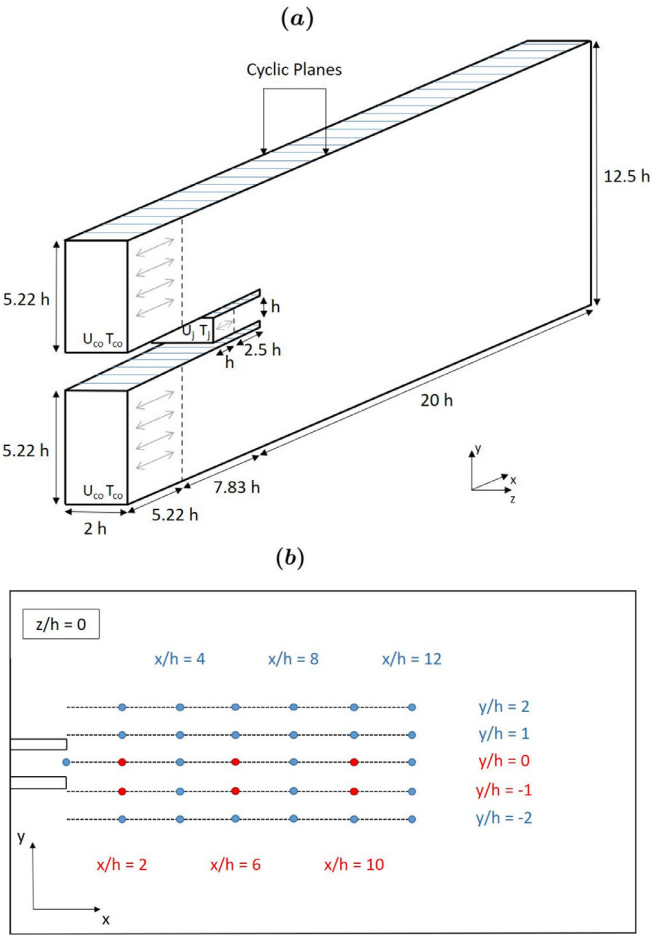

Fig. 1. Sketch of the computational domain (a) and distribution of monitor points (b).

3. Computational Details

3.1. Computational domain

The adequate computational representation of the wind tunnel test section and experimental inlet conditions were recently discussed in our previous work, where we have applied the RANS simulation approach, [18]. In the present study, we apply the most universal configuration containing three inlet periodic channels (pre-cursor simulations) representing the central jet and co-flow jets, which are mapped to the inlet plane of the simulation domain, as shown in Fig. 1(a). A network of monitoring points is distributed in the central vertical plane of the simulation domain to provide detailed insights into local spatial and temporal behavior of the velocity components and temperature, Fig. 1(b). The locations at which temporal spectra are analyzed in the present study are marked by red circles. The gravitational force effects are neglected due to a dominant forced convection flow regime with Reynolds and Richardson numbers, $\mathrm{Re} = 18000$ and $\mathrm{Ri} << 1$, respectively. The most important geometrical dimensions are the jet nozzle height $h = 0.02115$ m and jet-mixing domain length and height of 20h and 12.5h, respectively.

The special attention is devoted to obtain fully developed flows before entering the jet-mixing zone and limiting the total amount

Table 1
Mesh details of one pre-cursor co-flow channel.

Mesh	N_x	N_y	N_z	Total	$u_\tau[m/s]$	y^+	Δx^+	Δz^+
Standard	83	124	150	$1.51 \cdot 10^6$ CVs	0.18	0.88	37	3
Finer (f)	83	124	300	$3.02 \cdot 10^6$ CVs	0.18	0.88	37	1.5

Table 2
Mesh details of the pre-cursor jet channel.

Mesh	N_x	N_y	N_z	Total	$u_\tau[m/s]$	y^+	Δx^+	Δz^+
Standard	100	133	150	$2.0 \cdot 10^6$ CVs	0.81	0.71	39	15
Finer (f)	100	133	300	$3.02 \cdot 10^6$ CVs	0.81	0.71	39	7.5

of control volumes for an affordable computational costs[1]. For this purpose, several simulations are performed to optimize the channel numerical mesh and periodicity length. We found that the periodicity lengths of 1h and 5.22h for the pre-cursor jet and co-flow channels, respectively, provided required fully developed flow conditions. To avoid any artificial numerical interference of the jet flow, the mapping location of the imposed pre-cursor periodicity is kept at the same distance as in our previous RANS simulation of identical configuration, [18]. Furthermore, the width of the simulation domain is limited to 2h to achieve the adequate mesh criteria for the LES (see below). Knowing that specific features of the experimental setup design affected uniformity of the inlet co-flows velocity, we select the co-flow with the most uniform distribution of the mean inlet velocity, [18]. Then, for both co-flow inlets, a uniform velocity of $U_{co} = 3.15$ m/s is imposed. To keep the identical ratio of the mean flow rates of the central jet and co-flows as in experiments, the mean jet velocity of $U_J = 14.97$ m/s is imposed at the inlet of the pre-cursor periodic central channel.

We apply a two-step procedure for the specification of the initial turbulence fluctuations. In the first step, entire flow and pressure fields are interpolated from the previous three-dimensional RANS-type simulations, [18]. The reference mean streamwise velocity is imposed at the pre-cursor channel inlets with random perturbation of the fluctuating velocity components, [33]. In this initialization stage, the periodicity distance of the pre-cursor simulation was significantly shortened (i.e. only 1/10 of periodic length was simulated) to allow the random perturbations to survive. In the second phase, as soon as the velocity fluctuations (monitored in time) have reached the end of shortened pre-cursor subchannel, the random perturbations were switched off and the periodic length was set to the correct value.

At the outlet, the convective boundary condition is imposed for velocity. For the pressure, the zero-gradient boundary condition is applied at the inlets, while the zero value of the pressure is imposed at the outlet. The initial temperature of 298 K was set in the entire domain at the start of simulations. The jet and co-flow temperatures of $T_J = 299.1$ K and $T_{CO} = 311.1$ K were imposed to maintain the MYRTE wind tunnel experimental conditions ($\Delta T = T_{CO} - T_J = 12$ K temperature difference) for all the considered fluids. The zero-gradient temperature condition is applied at the outlet. At the side boundaries, the cyclic/periodic boundary conditions are imposed.

3.2. Mesh details

In the LES of a simple channel flow, the most demanding mesh resolution is in the proximity of walls. This mesh refinement is necessary to properly capture dynamics of the coherent turbulence structures (i.e. the quasi-streamwise vortices), [34]. The requirements of properly resolved turbulent boundary layers are $\Delta x^+ = 100$, $\Delta z^+ = 20$, and $y^+ \leq 1$, where the wall units are defined as $y^+ = u_\tau y/\nu$, [35]. The basic mesh contains in total 12.16 M control volumes, and a finer mesh (denoted as '(f)') is generated by doubling the mesh distribution in the spanwise z-direction. An overview of the most important mesh specifications is given in Tables 1, 2 and 3. Note that a non-dimensional characteristic averaged scale, defined as $\left(\overline{l_c} = \sqrt[3]{\frac{\text{Domain volume}}{\text{Control volumes}}}\right)$, is also provided. The special attention is devoted to have an adequate numerical resolution for both velocity and passive scalar (temperature) fields for various values of simulated Prandtl numbers. The characteristic Kolmogorov and Corrsin length scales, which are defined as

$$\eta = \left(\frac{\nu^3}{\epsilon}\right)^{\frac{1}{4}}, \quad \eta_\theta = \eta \ \mathrm{Pr}^{-\frac{3}{4}} \tag{26}$$

[38], are estimated from simulations. The characteristic dissipation rate is calculated as $\epsilon = \nu\left\langle\left(\frac{\partial u_i'}{\partial x_j}\right)^2\right\rangle$, with $u_i' = \hat{U}_i - \langle U_i\rangle$, where the long-term time-averaging ($\langle\ldots\rangle$) is performed during the simulation runtime. Contours of the characteristic ratio between the local control volume (CV) based length scale ($l_c = (\Delta_{CV})^{1/3}$) and temperature length scale (η_θ) are shown in Fig. 2. We kept constant value of the kinematic viscosity ($\nu = 1.55 \cdot 10^{-5}$ m^2/s), and adjust the thermal diffusivity in the temperature equation such that $\alpha = \nu/\mathrm{Pr}$. It can be seen that for Pr = 0.71 and Pr = 0.2, Figs. 2(a),(b), that we deal with a well-resolved LES for both velocity and temperature fields. In contrast to this, for Pr = 0.025 and Pr = 0.006, Figs. 2(c),(d), we have a fully resolved DNS for temperature field because of $l_c/\eta_\theta \leq 2$. It is noted that a proper $\Delta x^+/\Delta z^+$ proved to be essential for keeping an adequate numerical mesh for combined dynamic LES/DNS simulations over an entire range of Prandtl numbers.

Table 3
Mesh details of the jet-mixing domain.

Mesh	N_x	N_y	N_z	Total	$\overline{l_c}$[m]
Standard	100	477	150	$7.16 \cdot 10^6$ CVs	$6.79 \cdot 10^{-4}$
Finer (f)	100	477	300	$14.32 \cdot 10^6$ CVs	$5.39 \cdot 10^{-4}$

4. Results

4.1. Qualitative analysis of the flow and thermal fields

To get an impression of the flow morphology of the simulated case, instantaneous three-dimensional distributions of the total vorticity and velocity are shown in Fig. 3. The central high-velocity jet interacting with lower momentum co-flow jets pro-

[1] Numerical simulations were performed by using the ChemE computational cluster of the Applied Sciences Faculty at TUD.

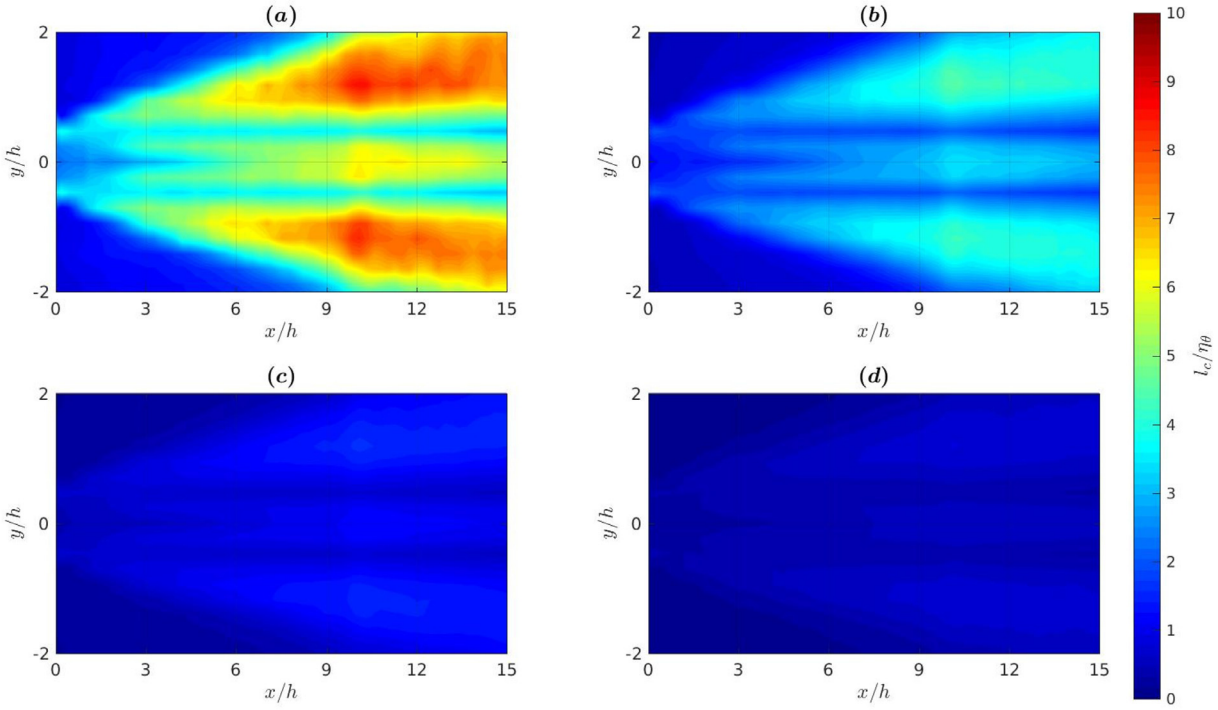

Fig. 2. Contours of characteristic computational control volume length to smallest temperature scale ratio (l_c/η_θ) at Pr = 0.71 (a), 0.2 (b), 0.025 (c) and 0.006 (d).

(a)

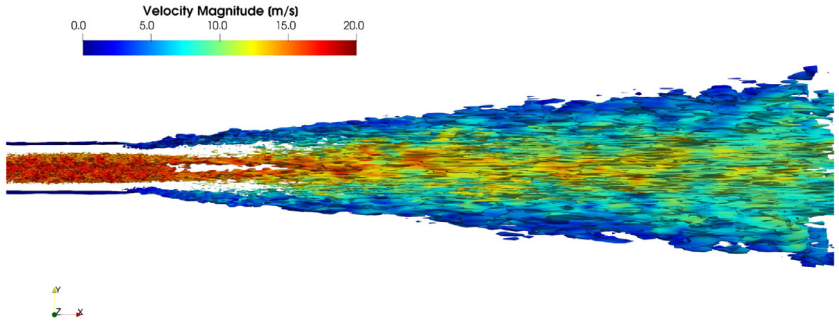

(b)

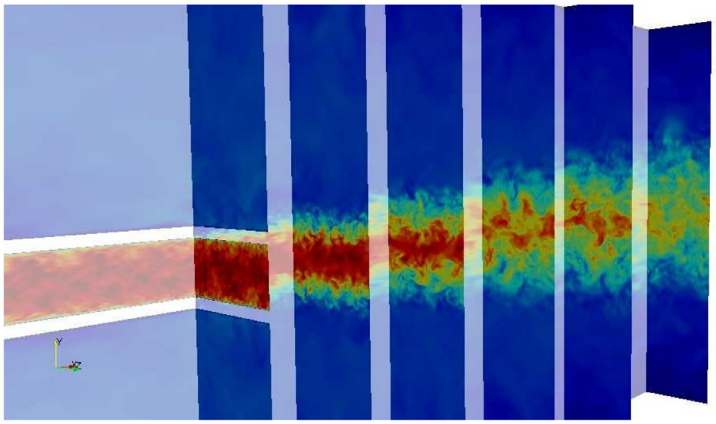

Fig. 3. (a) The isosurface of the instantaneous vorticity $\omega_z = 2$ kHz colored by the instantaneous velocity magnitude; (b) The contours of the instantaneous velocity magnitude in characteristic planes aligned and perpendicular to the jet direction.

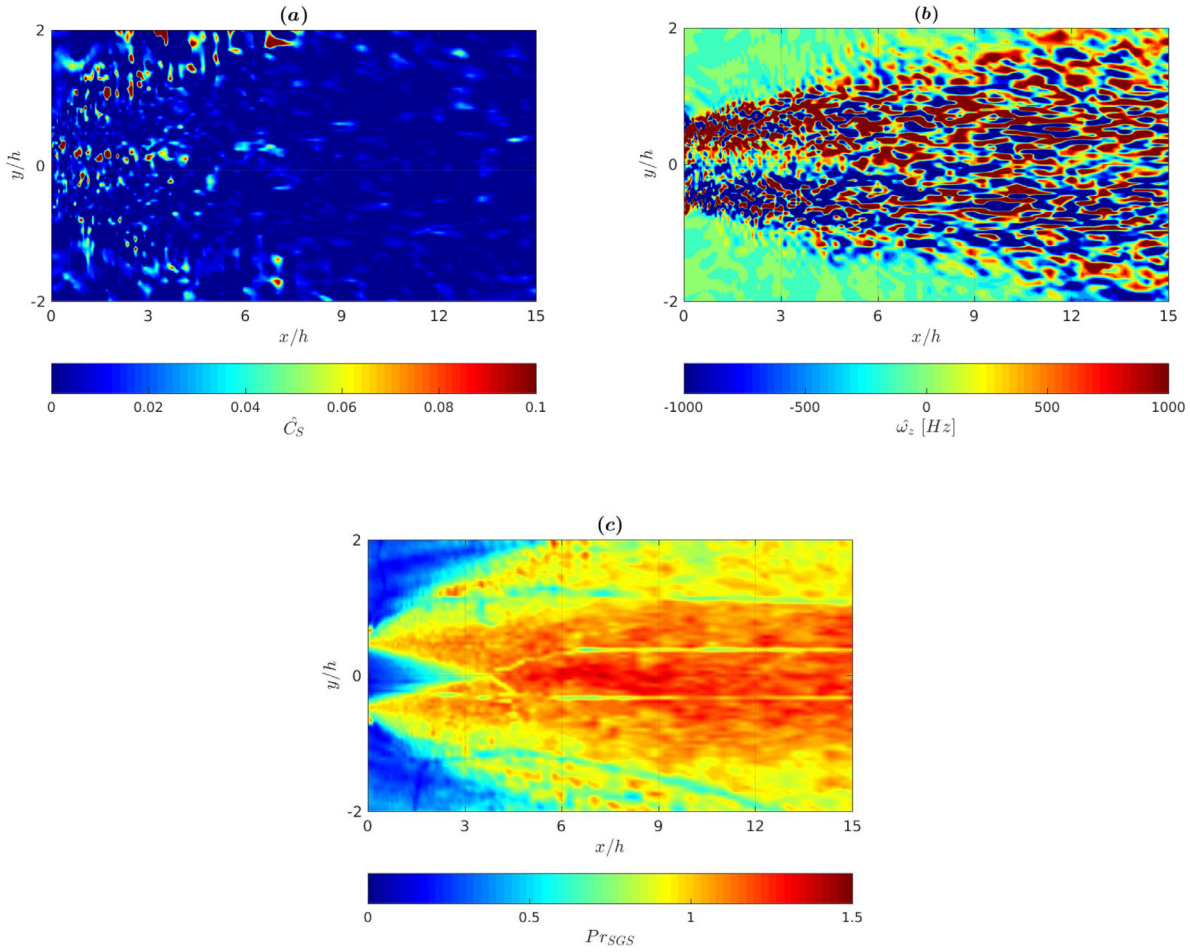

Fig. 4. Contours of instantaneous dynamically calculated Smagorinsky constant (C_s) (a), instantaneous spanwise vorticity component (b) and subgrid-scale turbulent Prandtl number (Pr_{SGS}) at $Pr = 0.71$ (c), in the central vertical plane ($z/h = 0$).

duces well defined shear-layers, Fig. 3(a). Contours of the instantaneous velocity in various vertical planes are shown in Fig. 3(b). Here, the process of intensive mixing in the spanwise direction can be observed resulting in continuous weakening of the central jet. Also, the interface between the highly intermittent central jet region and laminar-like region farther away from co-flows can be easily identified.

Contours of the dynamically calculated and locally averaged Smagorinsky constant in the central vertical plane are shown in Fig. 4(a). The contours of the instantaneous vorticity in the central vertical plane are shown in Fig. 4(b). The highest concentration of the vorticity can be found in the shear-layers, as well as in the wake of the side-walls separating the central jet and co-flow jets. The instantaneous flow features are a combination of the Kelvin-Helmholtz instability of strong shear-layers ([37]) and irregular reattachment of the weak regions behind the side-walls at the inlet plane (wake region) [36]. The contours of the locally calculated Pr_{SGS} (from Eqn.(21)) for the case with $Pr = 0.71$ are shown in Fig. 4(c). It can be seen that the local distribution exhibits a significant variation. Starting from small values in the proximity of inlets, the turbulent Prandtl number is close to one along the interface between the jet and outer co-flows, and finally, values larger than one are obtained in the core region of the central jet for $x/h > 3$.

The contours of the instantaneous streamwise velocity ($\overline{U_x}$) and long-term time-averaged turbulent kinetic energy in the central vertical plane are shown in Fig. 5. The interface between the high- and low-velocity regions is easily distinguishable from contours of the instantaneous streamwise velocity, Fig. 5(a). The contours of the turbulent kinetic energy ($k = 1/2\langle u_i^2 \rangle$) exhibit a characteristic initial double peak behaviour, which originates from a strong shear between the central and co-flow jets, as shown in Fig. 5(b). We will use these plots also to indicate local similarities and dissimilarities between the velocity and thermal field distributions for different values of the Prandtl number.

Distribution of the instantaneous temperature for different Prandtl numbers (in the same plane) are shown in Fig. 6. At Pr = 0.71 and Pr = 0.2 (Figs. 6(a) and (b)), the thermal fluctuations are primarily driven by the velocity fluctuations resulting in corresponding fine-scale thermal imprints. In contrast to this behavior, with further reduction in Prandtl numbers, for Pr = 0.025 and Pr = 0.006, Figs. 6(c) and (d), instantaneous temperature patterns exhibit more coarse-grained imprints, demonstrating increased importance of thermal diffusion (i.e. dampening of the thermal fluctuations).

Contours of the long-term time-averaged temperature variance ($k_\theta = 1/2\langle \theta^2 \rangle$) (again in the central vertical plane) are shown in Fig. 7. It can be seen that for Pr = 0.71 and Pr = 0.2 (Figs. 7(a) and (b)), that the highest values are located in shear-layers, because of the highest temperature differences. With the increase of the distance from the inlet plane, as a result of intensive mixing, values of

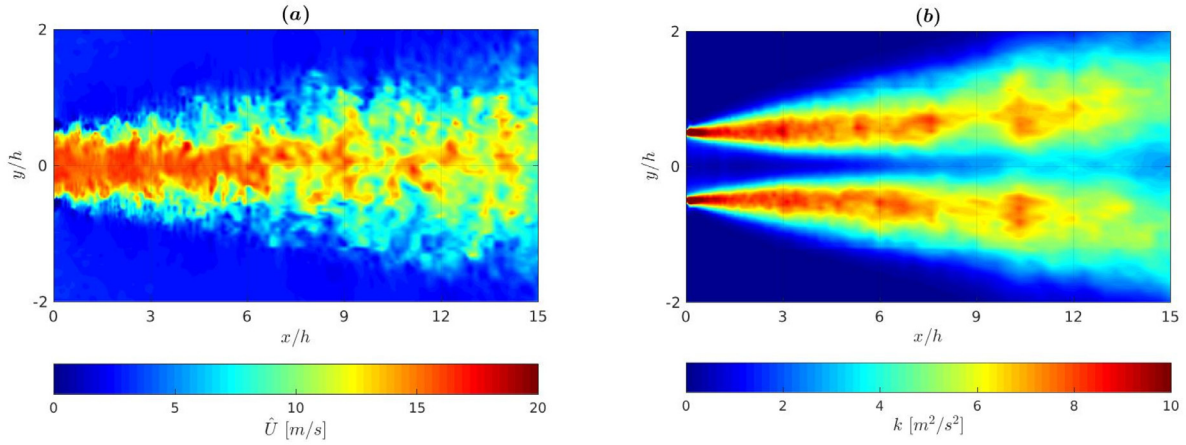

Fig. 5. Contours of the instantaneous streamwise velocity (a) and long-term time-averaged turbulent kinetic energy (b) in the central vertical plane ($z/h = 0$).

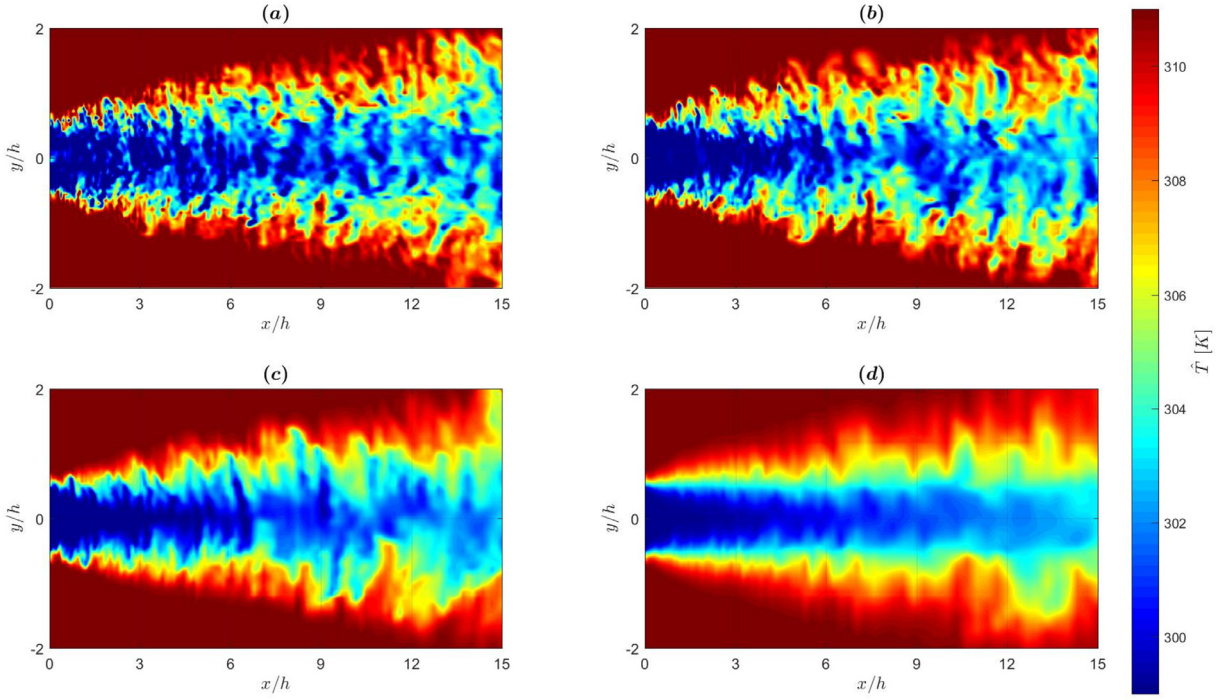

Fig. 6. Contours of resolved instantaneous temperature ($\hat{T}$) at Pr = 0.71 (a), Pr = 0.2 (b), Pr = 0.025 (c) and Pr = 0.006 (d).

the temperature variance are gradually decreasing. For lower values of Prandtl number, Pr = 0.025 and Pr = 0.006 (Figs. 7(b) and (c)), the behavior is different. The locations of the maximum temperature variance are moved farther downstream, $6 \leq x/h \leq 12$ for Pr = 0.025 and $9 \leq x/h \leq 12$, for Pr = 0.006, respectively. For the lowest simulated value of Pr = 0.006, instead of two distinct regions with high values of the temperature variance, a single region with its maximum along $y/h = 0$ is generated, Fig. 7(d). This is the result of an overly dominant molecular thermal diffusion mechanism of temperature field, which results in effective suppression of the thermal turbulence contribution.

4.2. Quantitative analysis of the flow field

Next, we analyze the flow field. The long-term time-averaged quantities are obtained by collecting statistics for more than 60 characteristic flow-through times (FFT)[2]. The velocity profiles are compared against the MYRTE wind-tunnel measurements (denoted as 'EXP') and results from our previous RANS-type simulations (denotes as 'RANS'), [18]. For the latter, we use results of recently developed low-Reynolds $k-\epsilon-\zeta-f$ and $k_\theta-\epsilon_\theta$ model. First, we demonstrate that fully-developed turbulence conditions are generated and properly maintained in the pre-cursor simulations, Fig. 8. It can be seen that both the log-law velocity profile (Fig. 8(a)) and the turbulent kinetic energy (Fig. 8(b)) agree very well with the reference DNS of [39], confirming a proper level of turbulence. This condition was adequate for both used numerical meshes on which

[2] The Flow-Through Time (FTT) is here defined as the time required by the massless fluid particle to move from the inlet to the outlet of the jet-mixing domain at the constant velocity of 14.97 m/s. This led to 1 FTT ≅ 0.03s.

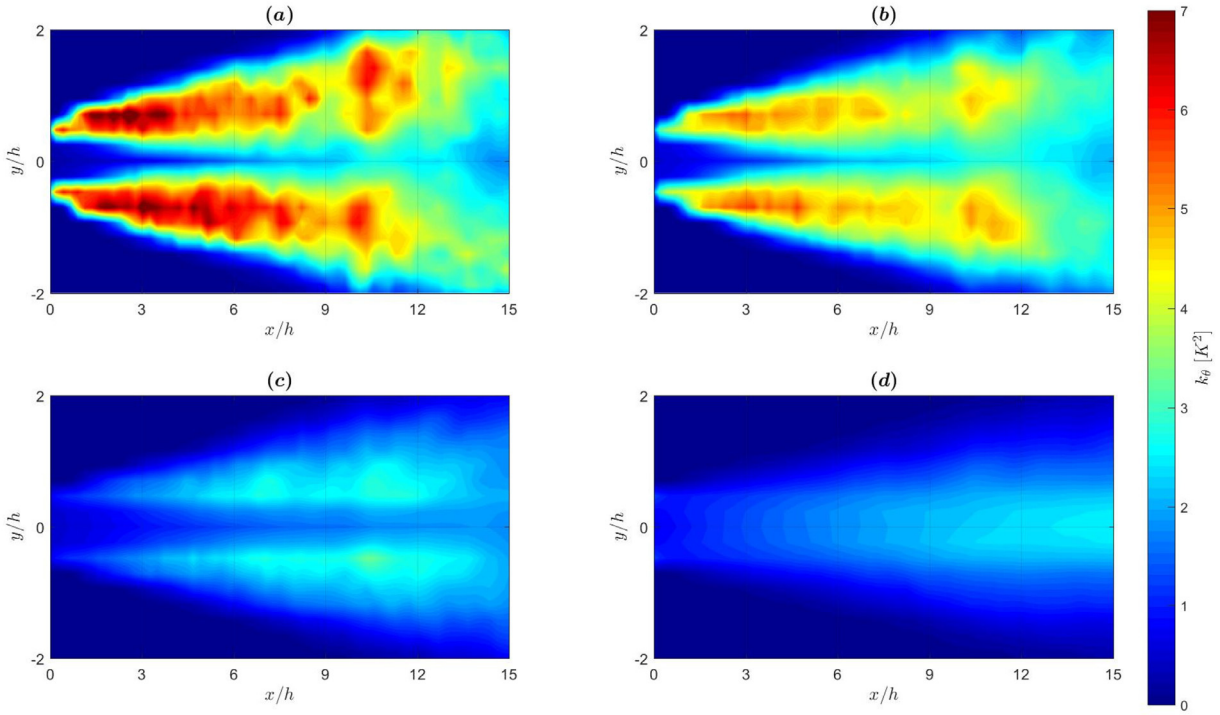

Fig. 7. Contours of long-term time-averaged temperature variance ($k_\theta = \langle\theta'\theta'\rangle/2$, where $\theta' = \hat{T} - \langle\overline{T}\rangle$) at Pr = 0.71 (a), Pr = 0.2 (b), Pr = 0.025 (c) and Pr = 0.006 (d).

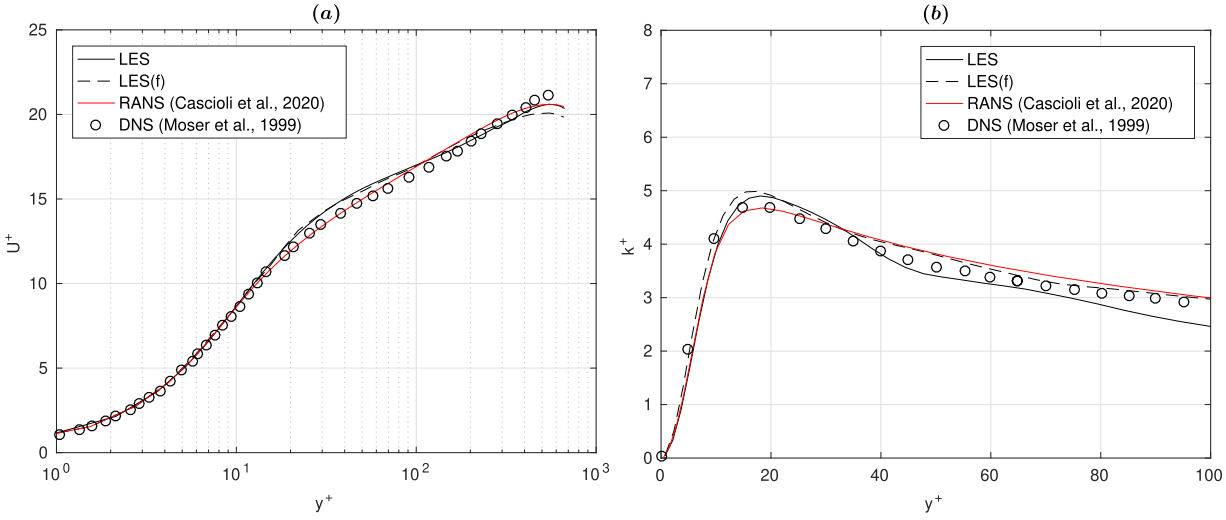

Fig. 8. Profiles of the log-law velocity (in the semi-log plot diagram, U^+ vs. y^+) (a), and the long-term time-averaged non-dimensional turbulent kinetic energy ($k^+ = \langle u_i' u_i' \rangle / 2u_\tau^2$, where $u' = \hat{U} - \langle\overline{U}\rangle$) (b), both at the half of the periodicity length in the pre-cursor jet channel.

the dynamic LES is performed, with a slight improvement for results obtained with the finer mesh (LES(f)) in the central part of the channel, Fig. 8(b).

Next, we compare profiles of the non-dimensional mean streamwise velocity ($U/(U_J - U_{CO})$) at different distances from the inlet, i.e. $x/h = 0, 5, 10$ and 15, respectively, as shown in Fig. 9. Exactly at the inlet plane ($x/h = 0$), there is a disagreement between the experiments and simulations due to some construction limitations of the inlet segment of the wind tunnel, [18]. These limitations resulted in an asymmetry between the two co-flow streams, at the sides of the jet. This asymmetry is eliminated by imposing fully-developed periodic boundary conditions in RANS and LES approaches. At $x/h = 5$ location, it can be seen that the LES produces significantly better agreement with experiments in comparison with the RANS, Fig. 9(b). The central peak value and jet spreading in the spanwise direction are well predicted. The RANS result shows weaker spreading and a higher peak in the jet center. The identical trend of the RANS and LES results is also present at locations farther downstream (i.e. at $x/h = 10$ and 15), Figs. 9(c) and (d). A good agreement between LES results on two different numerical grids also confirms the reliability of the presented dynamic LES approach.

From the profiles of the long-term time-averaged turbulent kinetic energy at the same locations ($x/h = 0, 5, 10$ and 15), it can be concluded that simulations show significantly higher values in comparison with experiments. To check to what extent this difference can be attributed to the two-dimensionality of the experimental approach, the missing averaged velocity fluctuations in the

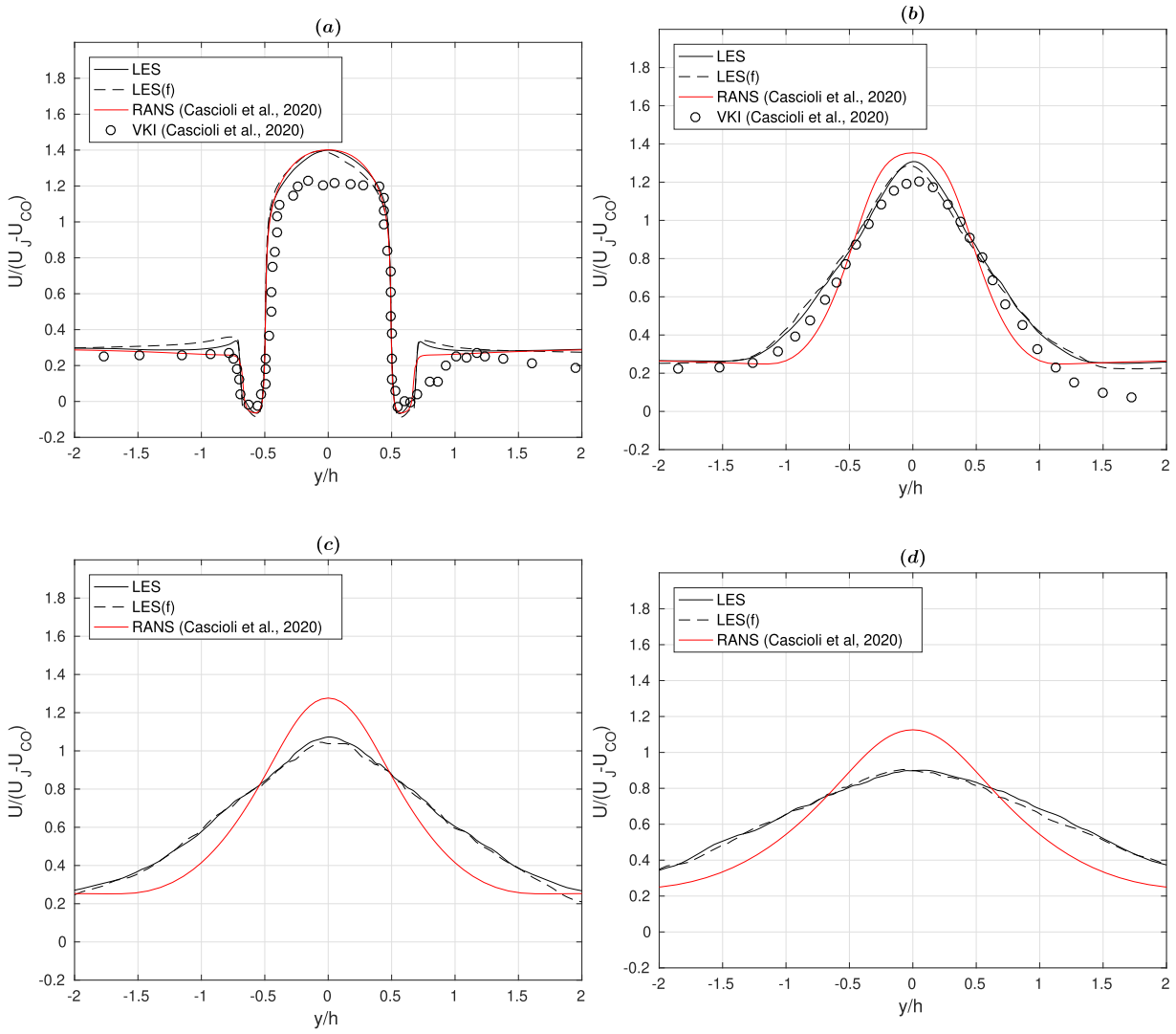

Fig. 9. Profiles of the long-term time-averaged streamwise velocity component $(\langle\overline{U_x}\rangle/(U_J - U_{CO}))$ at x/h = 0 (a), 5 (b), 10 (c) and 15 (d).

z-direction are omitted from the LES results (noted as LES(2D)) in Fig. 10). It can be seen that at $x/h = 5$ location, Fig. 10(b) resulted in a closer agreement between the LES and experiments, but the general overestimating trend is still present. Interestingly, the peak values of the reduced turbulent kinetic energy from LES are now closer to the peak values from the RANS model, but the spanwise distribution is still significantly higher, Fig. 10(b). Similar behavior is obtained at the $x/h = 10$, confirming more intensive turbulent mixing produced in LES in comparison with the RANS results. At $x/h = 15$, the profiles within the central jet region indicate similar trends between LES and RANS, whereas in the co-flow regions, the LES results again indicate stronger turbulence, Fig. 10(d).

The profiles of the resolved turbulent shear-stress are shown in Fig. 11. Again, the LES results show larger values compared to the RANS. At $x/h = 5$, both LES and RANS results are within the experimental data and in contrast to experiments, show proper symmetrical distributions, Fig. 11(b). At $x/h = 10$ location, almost identical peak values as at $x/h = 5$ are obtained for both simulations, Fig. 11(c). Finally, at $x/h = 15$, the peak values of the LES are reduced, and agreement between the LES and RANS is good in the central jet region, Fig. 11(d).

The profiles of the resolved turbulent shear stress at the same locations are shown in Fig. 11. At $x/h = 5$ location, the experimental data are between the RANS and LES results, Fig. 11(b). With further increase of the distance from the inlet, the RANS and LES results are getting closer, but the LES data indicate stronger turbulence in the co-flow regions.

Next we show profiles of the characteristic mechanical time-scale of the turbulence, i.e. $\tau_u = \langle k\rangle/\langle\varepsilon\rangle$, Fig. 12. it can be seen that a good agreement is obtained at the $x/h = 0$ and 5 locations, Figs. 12(a). This can be initially surprising since large differences between the turbulent kinetic energy calculated from the RANS and LES are indicated in Fig. 10(a). This larger value is accompanied also by a larger value of the dissipation, giving the final balanced outcome as shown in Fig. 12(a). The larger differences are obtained at the intermediate location, $x/h = 10$, where the RANS profiles indicate much larger values in the co-flow regions, Fig. 12(b). This can indicate low values of the dissipation (almost the laminar-like regimes), which in turn generates a large value of the mechanical time scale. This is followed by a very good agreement between the RANS and LES at $x/H = 15$, Fig. 12(b).

4.3. Quantitative analysis of the thermal field

We move next to analyze the temperature field. It should be noted that the dynamic SGS for the thermal part was activated only for the Pr = 0.71, whereas for the remaining Prandtl numbers, the numerical resolution was sufficient to fully resolve the typi-

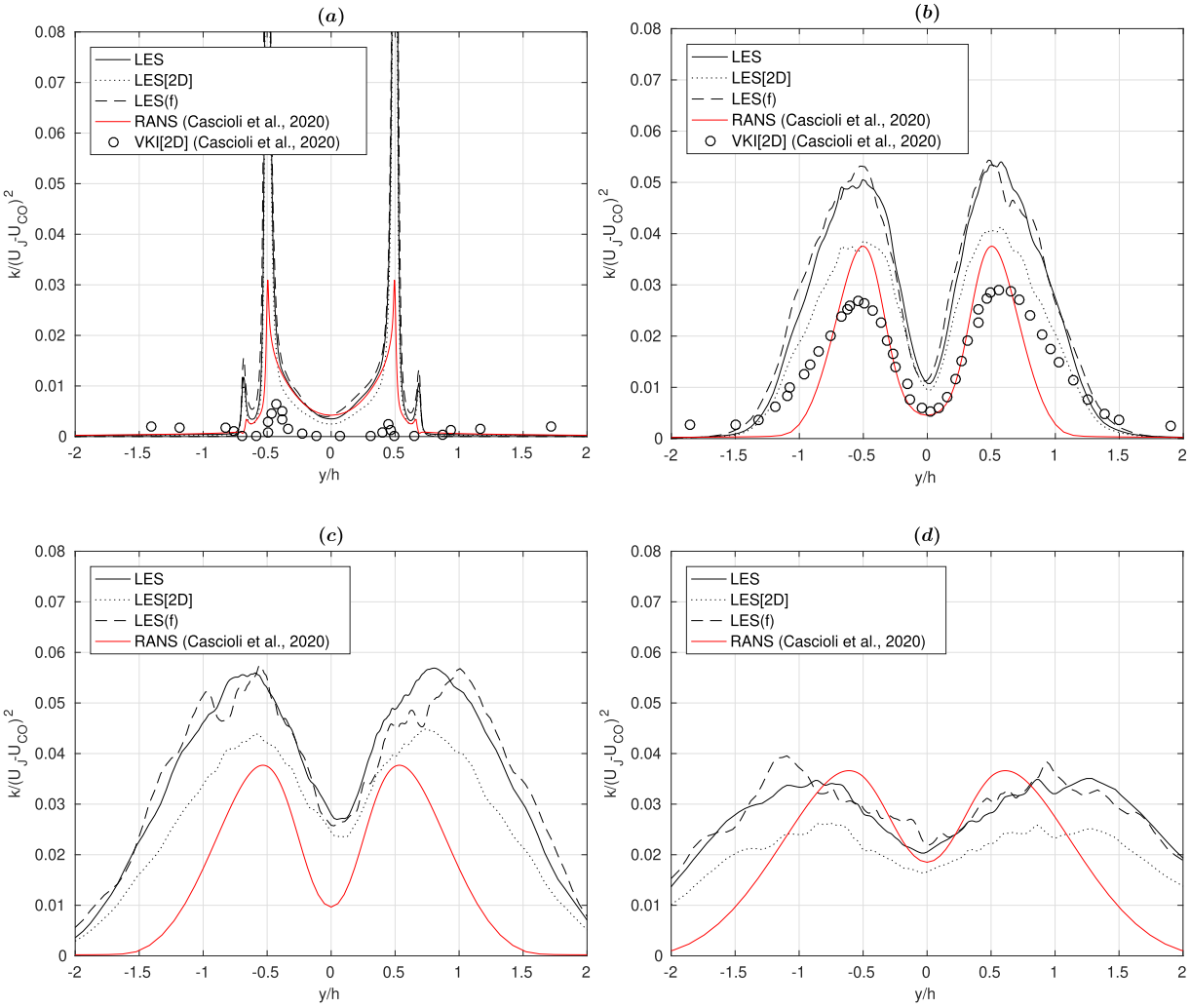

Fig. 10. Profiles of the resolved time-averaged turbulent kinetic energy at x/h = 0 (a), 5 (b), 10 (c) and 15 (d). Note that LES(2D) indicate the omission of the spanwise velocity fluctuations component, i.e. $k_{2D} = \frac{1}{2}\left(\langle u'u'\rangle + \langle v'v'\rangle\right)$ where $u' = \hat{U} - \langle\overline{U}\rangle$.

cal thermal scales, so we have a hybrid LES/DNS approach for velocity/temperature field, respectively. The resolved long-term time-averaged temperature profiles are shown in Fig. 13. Effect of changing Prandtl number on temperature profiles is rather small. Note that the RANS results are shown only for Pr = 0.2 for which experimental data are available. It can be seen that the current LES/DNS profile at the $x/h = 5$ is closer to experimental values in comparison with the RANS results, Fig. 13(b). The central jet peak value, as well as the spanwise spreading of the temperature, are well captured with the LES/DNS. The RANS profile shows a significant overestimation of the peak value in the jet center and narrower distribution in the spanwise direction. This trend of the RANS profile is kept at other locations too, i.e. $x/h = 10$ and 15, Figs. 13(c) and (d). At these locations, the LES/DNS results indicate that Prandtl number effects are primarily visible in the jet center, with significantly smaller differences in the co-flow regions. This additionally confirms that molecular diffusion plays a small role in the distribution of the temperature profiles, where the convective and turbulence contributions are more important.

The characteristic profiles of the non-dimensional temperature standard deviation are shown in Fig. 14. Single peak distributions are obtained for the lowest value of Pr = 0.006 already at $x/h = 5$, while the double peak distributions are obtained for remaining Prandtl numbers up to $x/h = 10$ location. At the $x/h = 15$, the central jet values are identical for all simulated Prandtl numbers (obtained with the LES/DNS approach), whereas the RANS profile still exhibits the double peak distribution, confirming a weaker mixing.

The profiles of the resolved vertical turbulent heat flux profiles are shown in Fig. 15. Farther away from the inlet location, a distribution with two characteristic peaks is obtained for all simulated Prandtl numbers. Also, a monotonically decreasing intensity of the turbulent heat flux proportional to the decrease in the Prandtl number is visible at $x/h = 5$ and 10, Figs. 15(b) and (c). At the final $x/h = 15$ location, the values in the center of the jet are very similar, and relatively small differences are still present in the co-flow regions, Fig. 15(d).

The profiles of the characteristic thermal time-scale ($\tau_\theta = \langle k_\theta\rangle/\langle\varepsilon_\theta\rangle$) are shown in Fig. 16. At both locations (i.e. $x/h = 5$ and $x/h = 10$), profiles exhibit a gradual reduction in the co-flow regions with the Prandtl number decrease. In contrast to this behavior, in the center of the jet, the values are initially suppressed, but for the lowest value of the Prandtl (Pr = 0.006), the peak value increased and is close to the result of the Pr = 0.71, Figs. 16(a). At $x/h = 10$, variations in the time-scale are significantly reduced, and with characteristic dominant peak in the jet center for the for Pr = 0.006, Fig. 16(b). This is a consequence of the single-peak behavior of the temperature variance (as previously shown in Fig. 7(d)). For both locations, the profiles of the thermal time-scale obtained

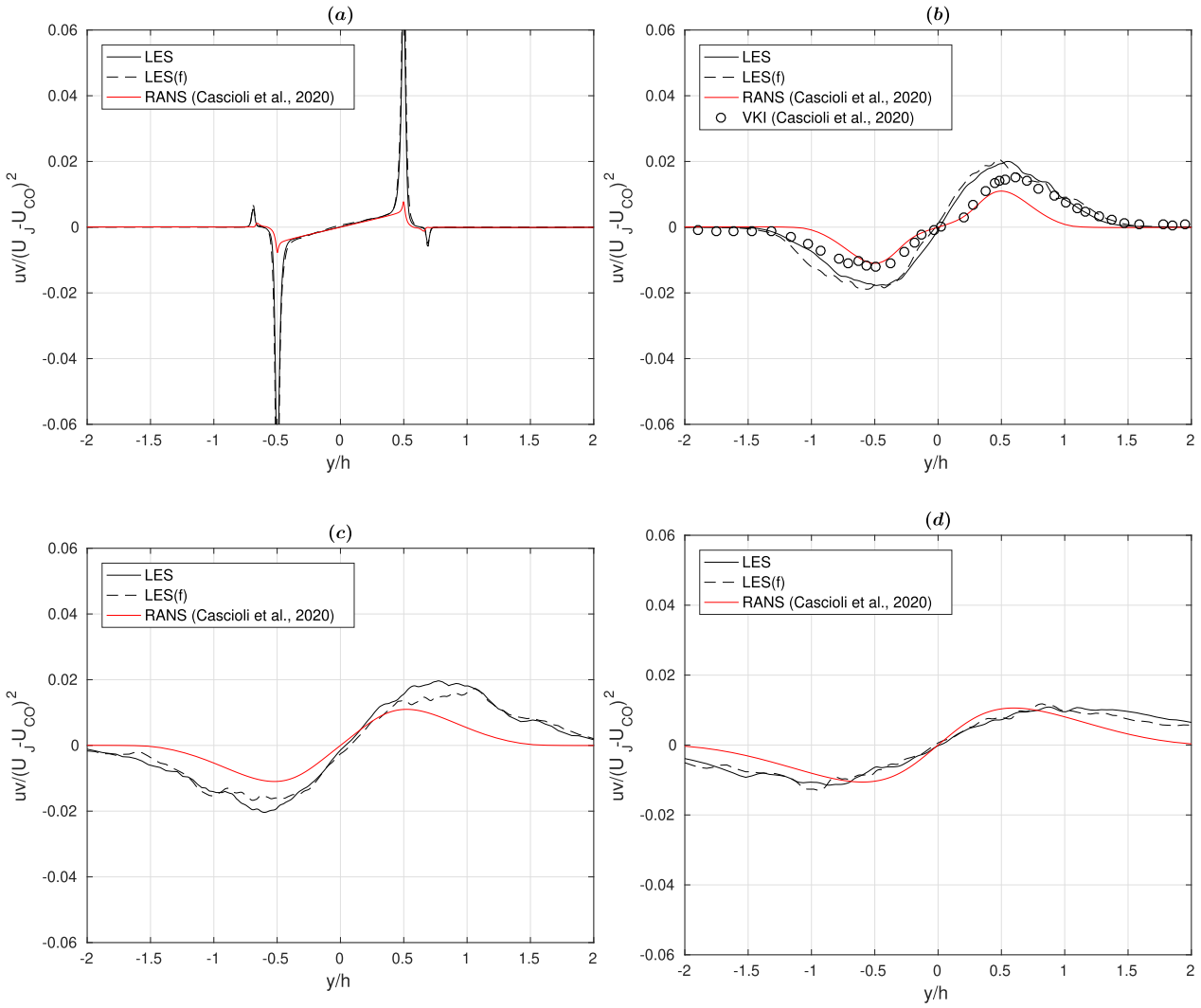

Fig. 11. Profiles of the resolved time-averaged Reynolds shear stresses at x/h = 0 (a), 5 (b), 10 (c) and 15 (d).

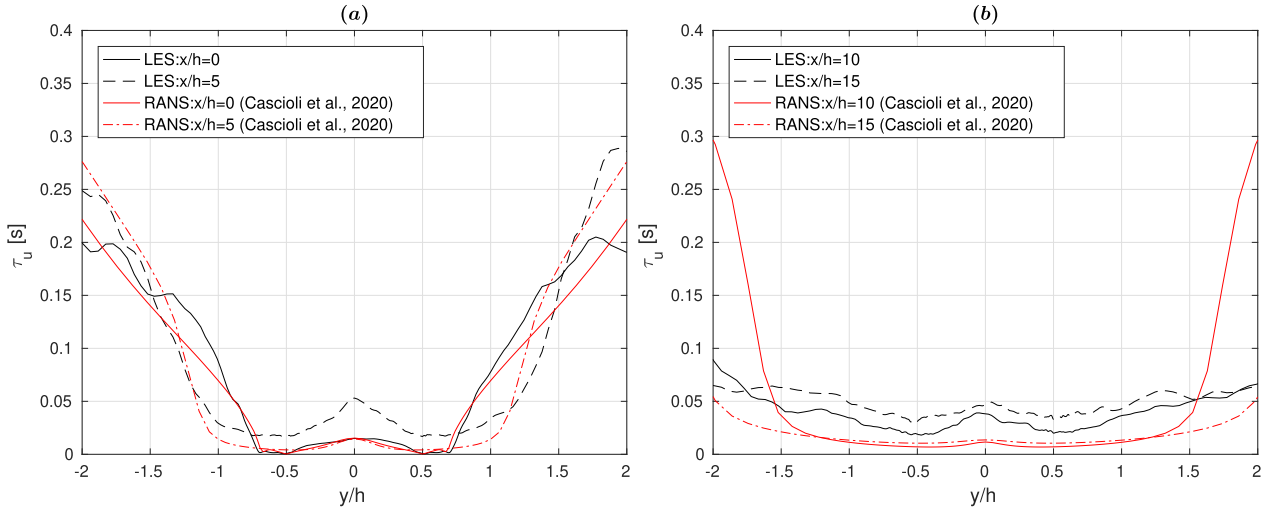

Fig. 12. Profiles of resolved time-averaged dynamical time-scales in the convergent (a) and self-similar (b) regions of the jet.

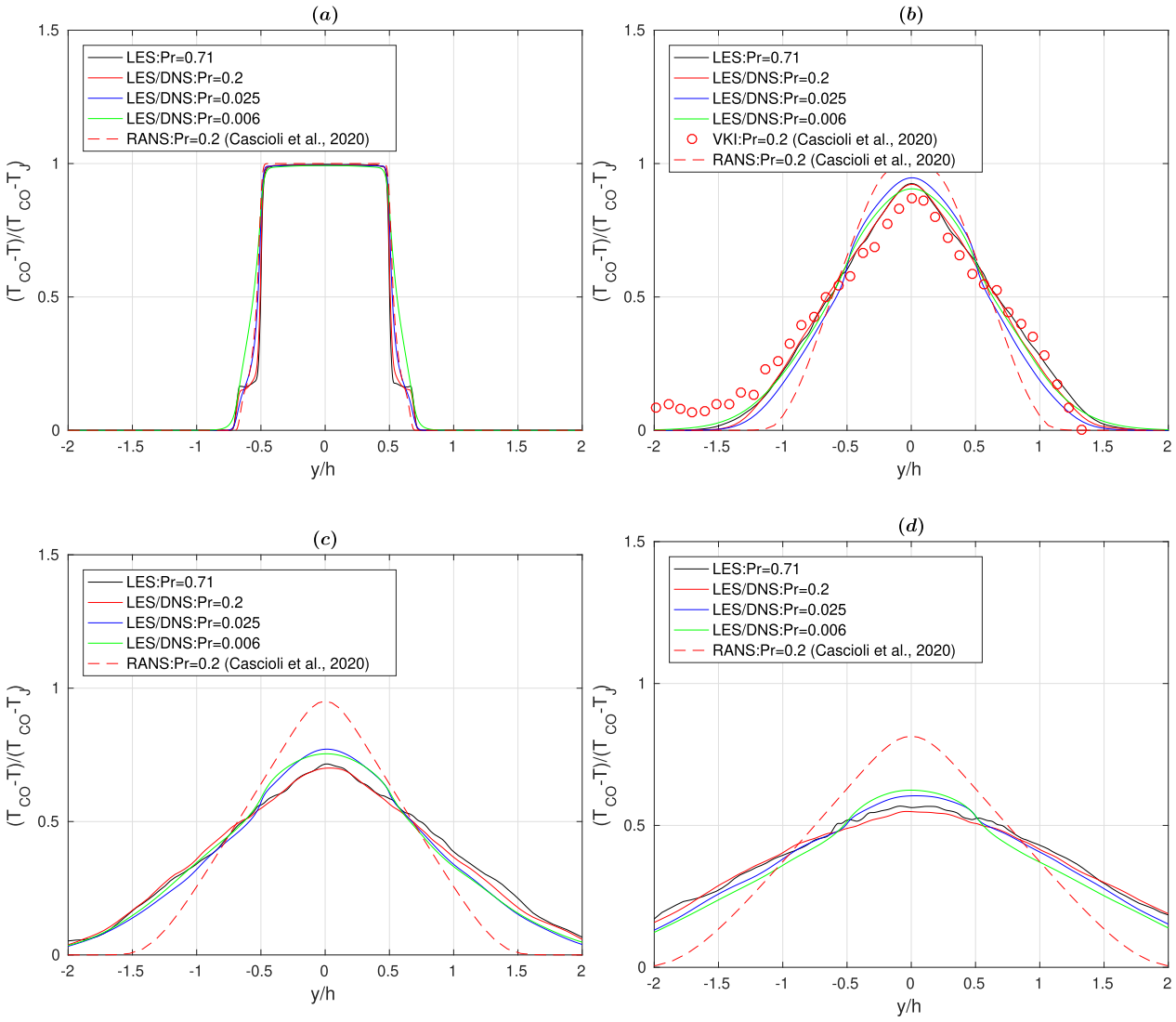

Fig. 13. Profiles of resolved time-averaged temperature at x/h = 0 (a), 5 (b), 10 (c) and 15 (d).

from the RANS model of [18] are also extracted for Pr = 0.2. It can be seen that a significant underprediction of the model is obtained for both locations, indicating a crucial point for its further improvement. Finally, the profiles of the time-scale ratio (defined as $R = \tau_\theta/\tau_u$) are shown in Fig. 17. It can be seen that relatively uniform distributions are obtained for LES at $x/h = 5$ location for Pr=0.71 and 0.2, Fig. 17(a). For lower values of the Prandtl number (Pr = 0.025 and 0.006), at the same location, a non-uniform distribution with a distinct peak in the centre of the jet is obtained. At $x/h = 10$ location, the LES distributions exhibit a non-uniform distribution for all considered values of Prandtl number, Fig. 17(b). Again, for Pr=0.025 and 0.006, a distinct peak in the jet centre is obtained. The RANS-based results of the time-scale ratio for Pr=0.2 exhibit characteristic two-peak behaviour at both locations, [18]. It can be seen that a large discrepancy is obtained in the jet centre and in the co-flow regions at $x/h = 5$ location, Fig. 17(a). A double peak behaviour shows values closer to the LES at $x/h = 10$, but locations in the jet centre and co-flow regions are still significantly underpredicted, Fig. 17(a).

The streamwise evolution of the typical shear layer thickness in the central vertical plane is shown in Fig. 18(a), demonstrating a good agreement between the LES and RANS. The profiles of the long-term time-averaged turbulent Prandtl number (calculated as $\mathrm{Pr_t} = \left(\overline{uv}dT/dy\right)/\left(\overline{\theta v}dU/dy\right)$) at $x/h = 10$ are shown in Fig. 18(b). It can be seen that a constant value of $\mathrm{Pr_t}$ (usually assumed in two-equation $k-\varepsilon$ models) of $\mathrm{Pr_t} = 0.86$ is a reasonable approximation for Pr=0.71. In contrast, for lover values of molecular Prandtl number, $\mathrm{Pr_t}$ profiles exhibit non-uniform distributions with characteristic peaks at $y/h = -0.5$ where the resolved shear-stress reaches its maximum. For Pr=0.025, the $\mathrm{Pr_t} = 1$ is a reasonable approximation except already mentioned peaks at $y/h = -0.5$ with a maximum value of $\mathrm{Pr_t^{max}} = 3$. For the lowest value or Pr=0.006, there is no segment with a constant value and its peak value is approximately $\mathrm{Pr_t^{max}} = 10$. This additionally stresses importance of designing the RANS-closures to take into account this highly non-uniform behaviour of Pr_t for low Prandtl fluids. It is interesting to observe that the six-equation RANS closure of [18] at Pr=0.2 agrees well with LES in the $-1 \le y/h \le 0$ region, whereas an overprediction is obtained in the co-flow region ($-2 \le y/h \le -1$).

4.4. Frequency-based power spectra

To collect time-series of fluctuating velocity and temperature, a dense network of monitoring points is introduced in the central

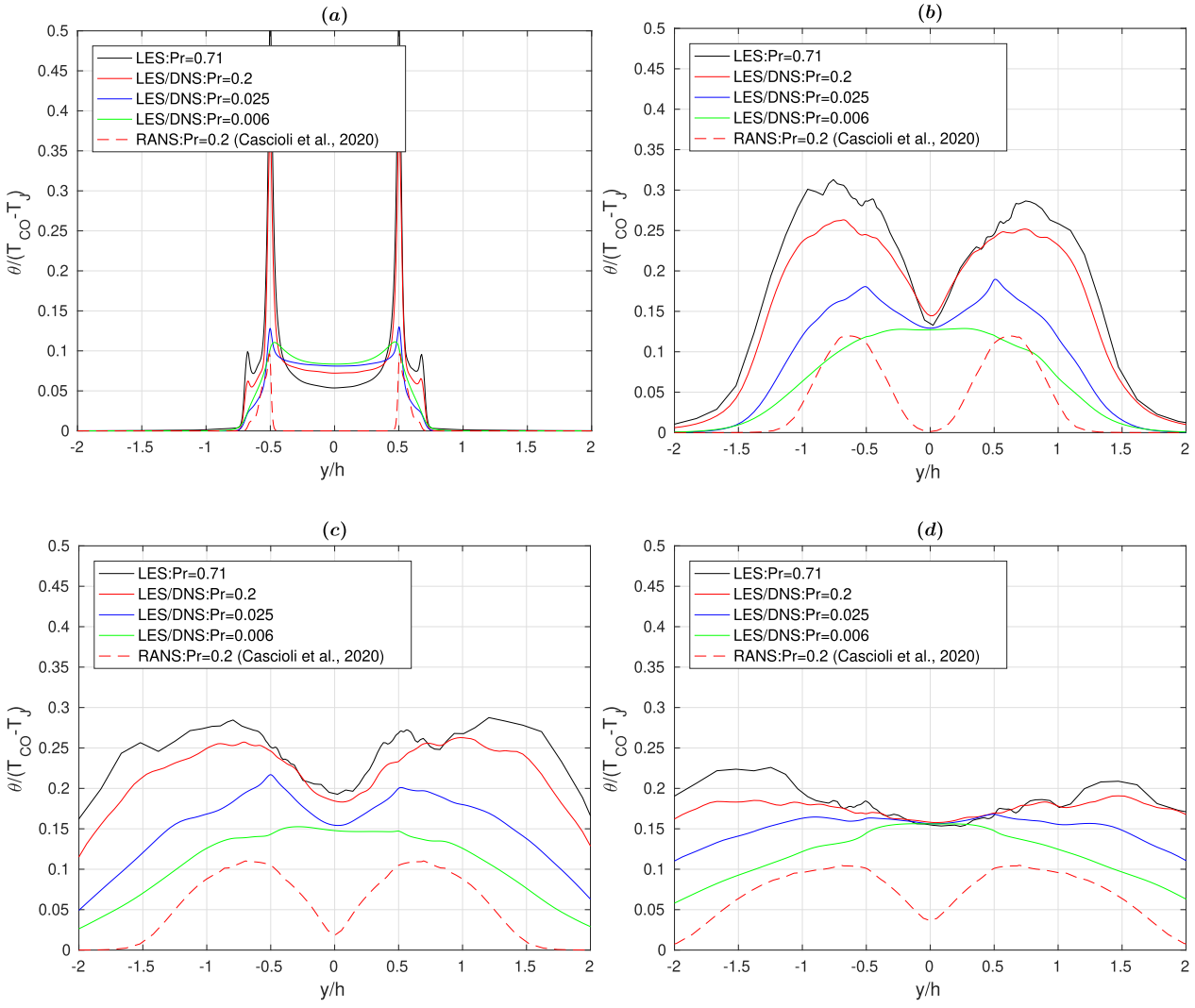

Fig. 14. Profiles of the non-dimensional standard deviation of temperature at x/h = 0 (a), 5 (b), 10 (c) and 15 (d).

vertical plane of the computational domain, as shown in Fig. 1(b). For selected number of locations extracted along the jet centerline ($y/h = 0$) and along the edge of the initial central jet ($y/h = -1$), we performed a discrete Fourier transformation to get the characteristic power-spectral density, Figs. 19 and 20. The fluctuating streamwise velocity spectra ($E_u(f) = \frac{1}{2}u'u'$, where $u' = \hat{U} - \langle\overline{U}\rangle$) is plotted in Fig. 19. The spectra of the fluctuating streamwise velocity at monitoring points extracted along the jet centerline ($y/h = 0$ and x/h =2, 6 and 10) are shown in Fig. 19(a). The presented spectra clearly indicate transitions between the energy-containing, convective-inertial, and viscous-dissipative ranges, [3]. It can be seen that for the frequencies up to $f = 1$ kHz, there is a continuous increase in the amplitude (E_u) with increasing distance from the inlet. There is a relatively narrow inertial range ($E_u \propto f^{-5/3}$, [40] in $0.5 \leq f \leq 2 \times 10^3$ kHz), followed by a rapid dissipation range ($E_u \propto f^{-8}$ in $2 \leq f \leq 6$ kHz) at $x/h = 6$ and 10, and finally, with a less steep decay up to $f = 200$ kHz. At the monitoring point closer to the inlet ($x/h = 2$), the rapid decay covers $2 \leq f \leq 7$ kHz range, followed with a milder decay range starting at $f = 10$ kHz and ending at $f = 200$ kHz.

The spectra of the monitoring points along the $y/h = -1$ line exhibit different behavior, Fig. 19(b). Compared to the centerline points, a significantly larger inertial ($f^{-5/3}$) range can be observed. The inertial range starts at $f = 200$ Hz and extends up to $f = 6$ kHz for the $x/h = 10$ location. In contrast to the significantly extended inertial range, the rapid-decay (f^{-8}) range is significantly reduced. At the $x/h = 6$ location, it extends between $f = 3$ and 6 kHz, whereas at $x/h = 10$, this range is between $f = 5$ and 7 kHz.

In analysis of temperature fluctuations ($E_\theta(f) = \frac{1}{2}\theta'\theta'$, where $\theta' = \hat{T} - \langle\overline{T}\rangle$) spectra, we selected only the highest (Pr = 0.71) and lowest (Pr = 0.006) values of Prandtl number, Fig. 20. For air (Pr = 0.71), at $x/h = 2$ and $y/h = 0$ (the jet centerline), distribution shows a close resemblance with the velocity spectra at the Fig. 20(a). The similarity with the velocity is also obtained in the energy-dominant regime ($f \leq 1$ kHz) at locations $x/h = 6$ and 10. The differences are again noticeable in the viscous-dissipation regimes, where the behavior at $x/h = 6$ is now closer to the $x/h =$ 2 than to $x/h = 10$. At the same locations, the temperature spectra for the Pr = 0.006 show similar behavior, but the amplitude E_θ is just shifted vertically to lower values, Fig. 20(c). At the off-center locations, i.e. $y/h = -1$, the temperature spectra of both Pr = 0.71 and Pr = 0.006 show significantly different distributions compared to the velocity spectra, Figs. 20(b) and (d). The amplitude E_θ now extends over a significantly larger range of almost ten decades at the off-center locations, but the maximum of the E_θ is significantly lower for Pr = 0.006.

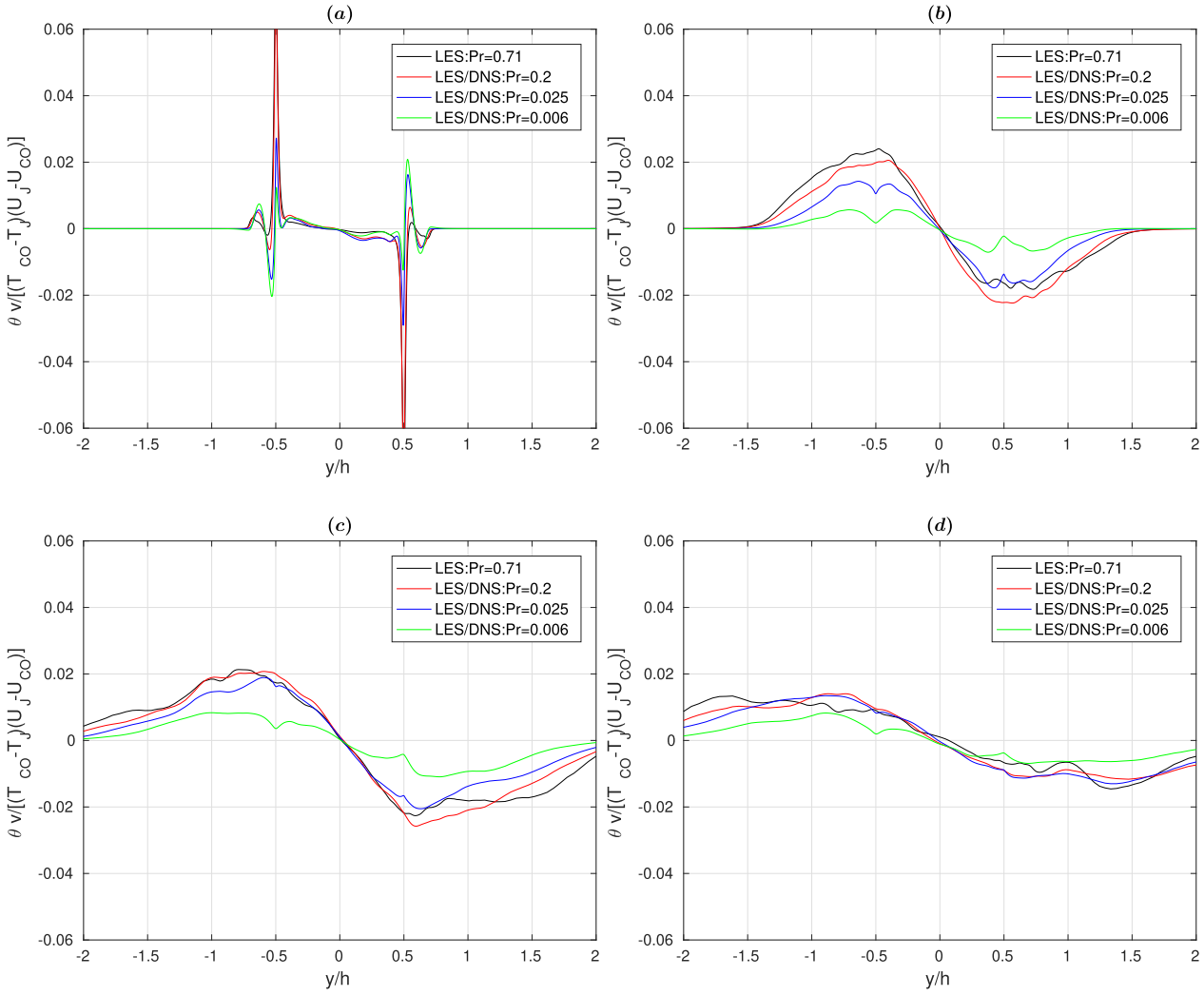

Fig. 15. Profiles of resolved time-averaged turbulent heat fluxes at x/h = 0 (a), 5 (b), 10 (c) and 15 (d).

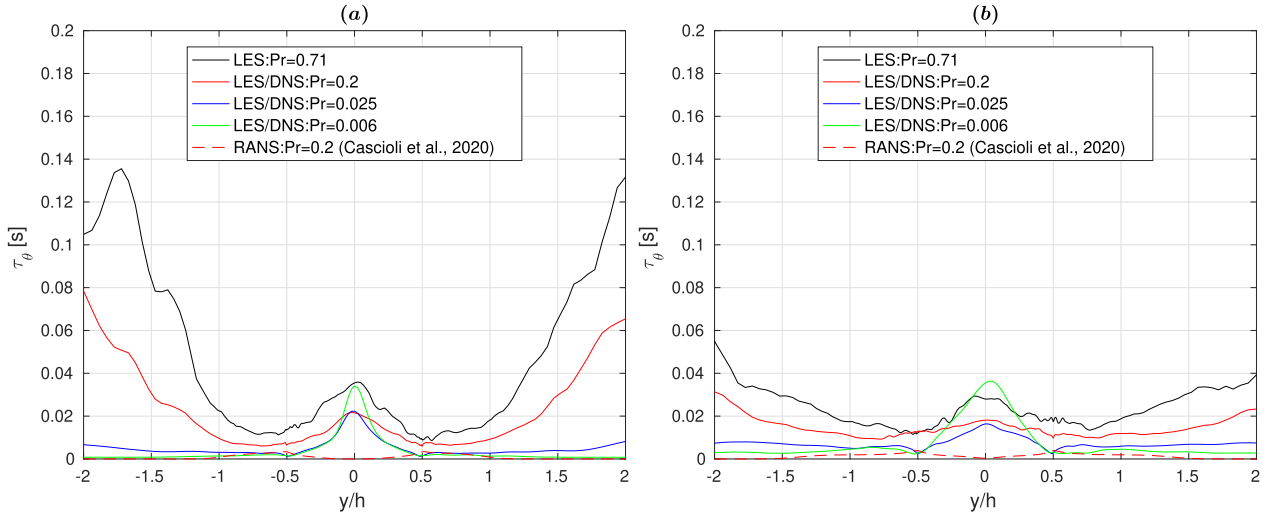

Fig. 16. Profiles of resolved time-averaged thermal time-scale at at x/h = 5 (a) and 10 (b).

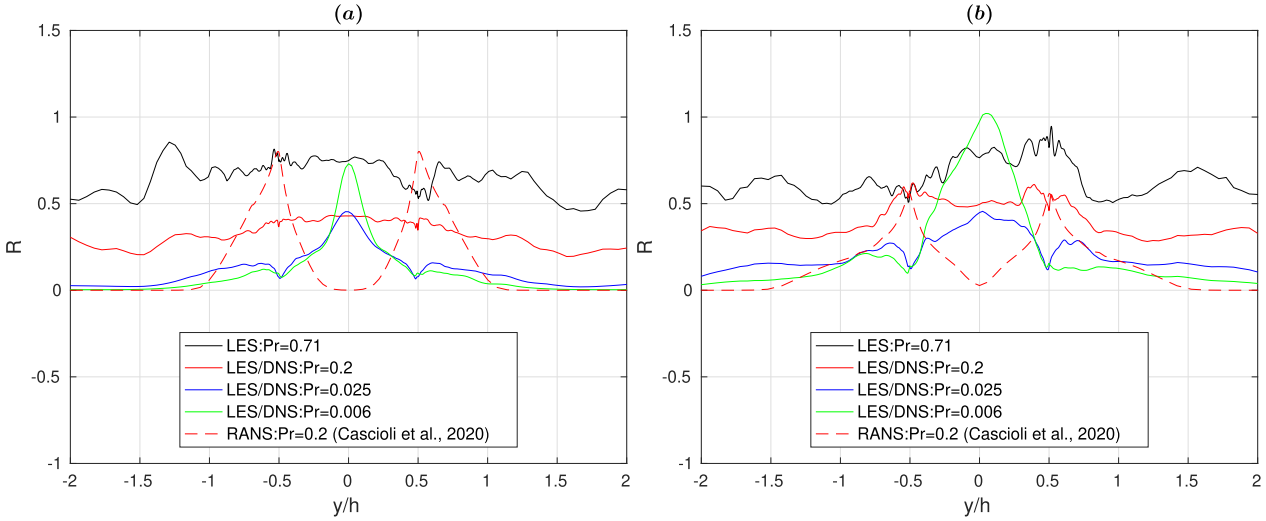

Fig. 17. Profiles of resolved time-scale ratio ($R = \tau_\theta/\tau_u$) at at x/h = 5 (a) and 10 (b).

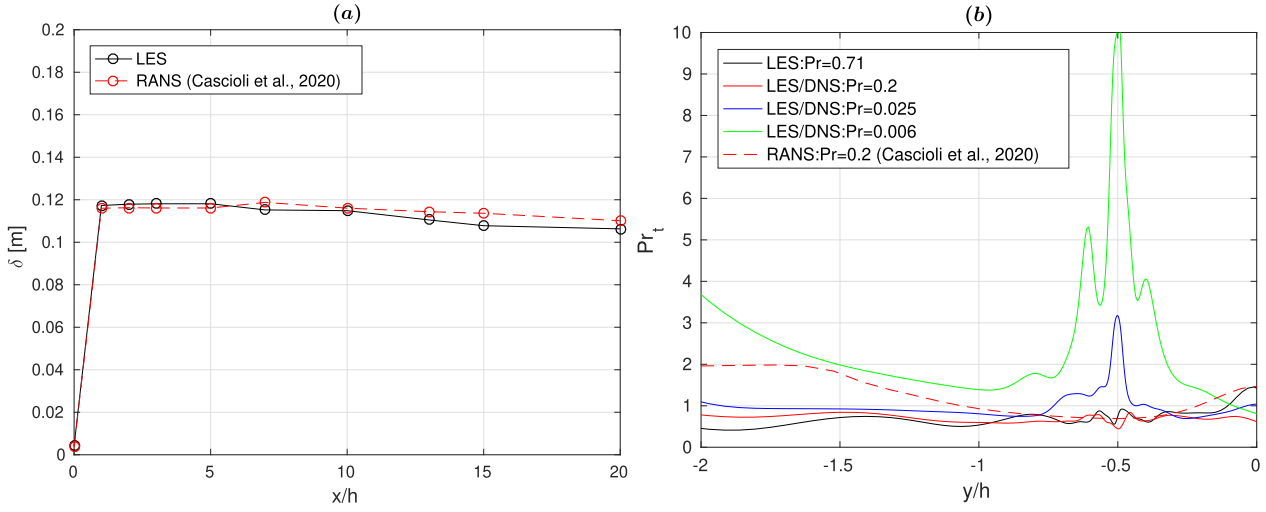

Fig. 18. Distribution of the shear-layer thickness (δ) in the streamwise direction (a), and zoom-in profiles of the turbulent Prandtl number (Pr_t) at $x/h = 10$ for various values of Pr.

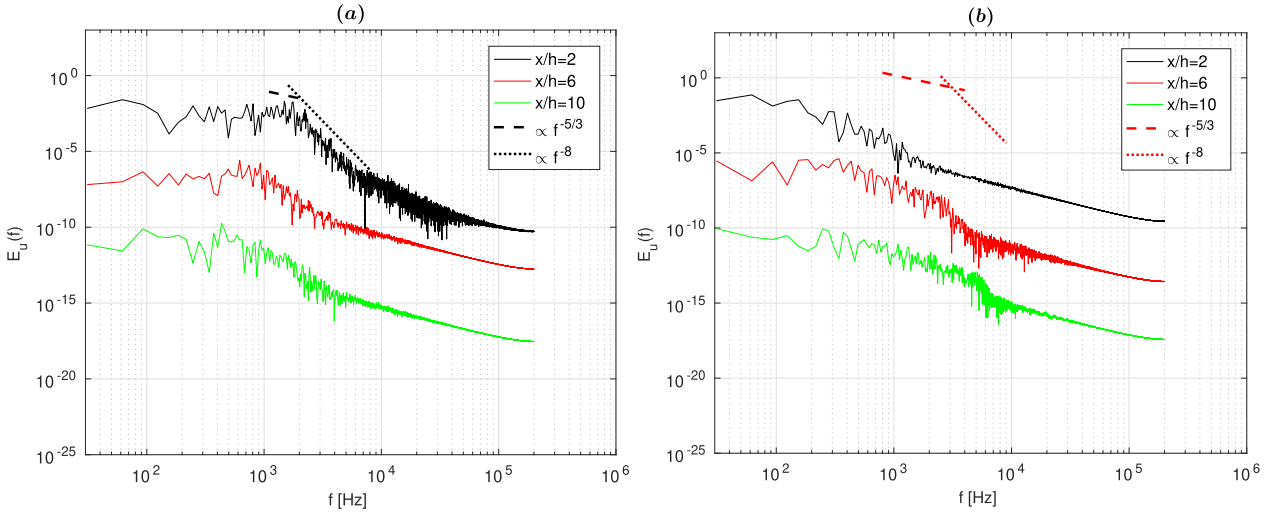

Fig. 19. The power spectra of the streamwise velocity component at the following monitoring point locations: y/h = 0 (a) and -1 (b) and z/h = 0 - Note that, because of the readability purposes, the red and green profiles have been systematically shifted by dividing the original signals by factors 10^5 and 10^{10}, respectively.

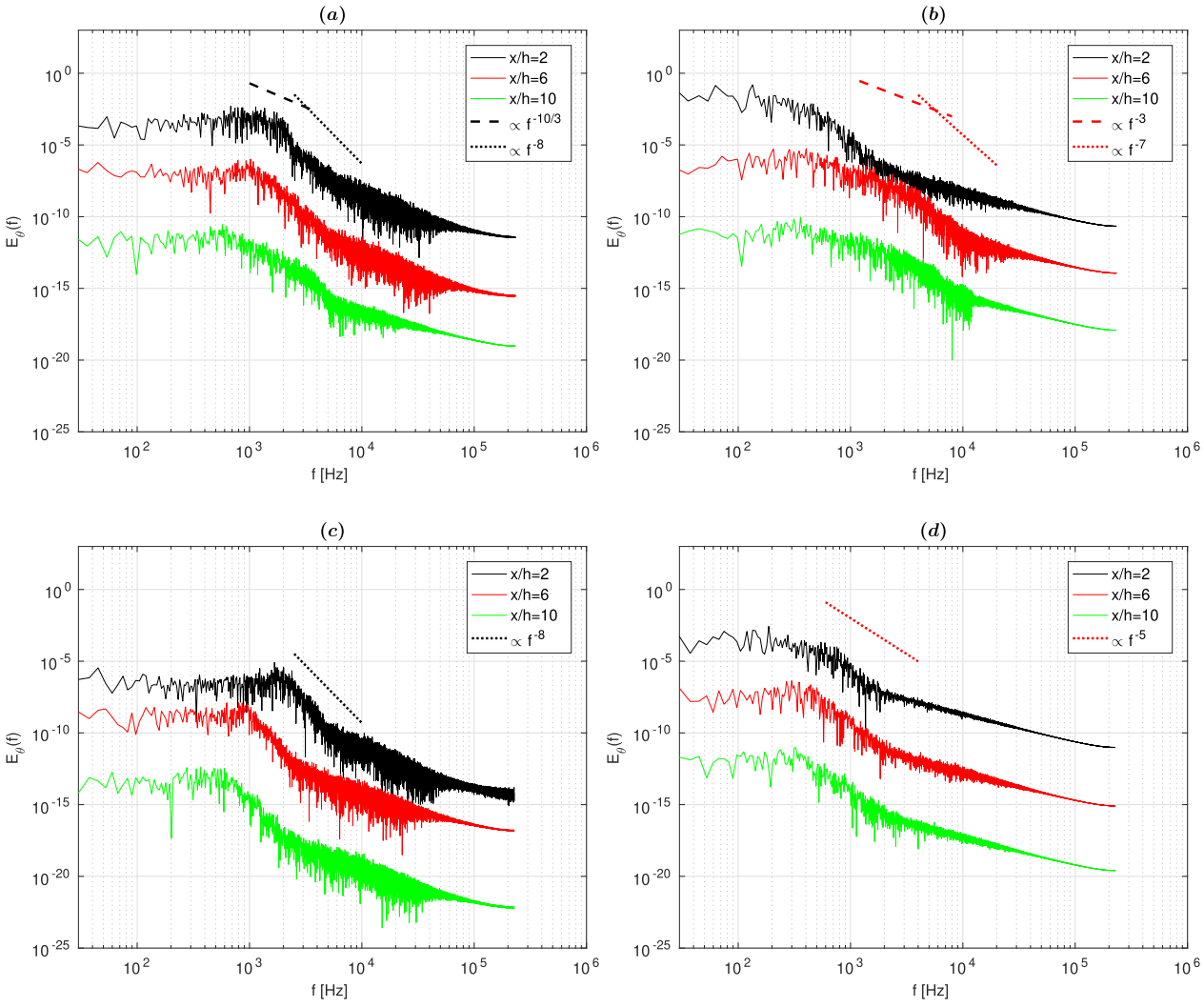

Fig. 20. The power spectra of the temperature for Pr = 0.71 (a,b) and Pr = 0.006 (c,d) at the following monitoring point locations: y/h = 0 (a,c) and -1 (b,d) and z/h = 0 - Note that, because of readability purposes, the red and green profiles have been systematically shifted by dividing the original signals by factors 10^5 and 10^{10}, respectively.

5. Conclusions

We performed fully dynamic LES and combined dynamic LES/DNS simulations of the forced convection planar jet under similar conditions as in recent experiments in the MYRTE wind tunnel operated at the VKI. To eliminate some of the design limitations of the experimental setup, which is resulting in asymmetrical inlet conditions, we impose pre-cursor simulations of the central jet and co-flows such that the typical flow rate ratios are identical to experiments. This approach proved to be numerically efficient and provided the fully developed turbulence in good agreement with DNS results from the literature. The obtained results were in good agreement with experiments regarding the mean velocity and temperature profiles. The current approach demonstrated significant improvement in predictions of the mean temperature profile in comparison to the four-equation RANS model, particularly with regards to the spanwise spreading of the jet. The mean temperature profiles demonstrated low sensitivity to changes of the Prandtl number. This is due to dominant mechanisms of convection and turbulent diffusion over molecular diffusion. Here presented results of the second-moments of the velocity and temperature fields can be used for detailed validation of the RANS-type models. Within the framework of the model validations, the here presented characteristic time-scale ratios and corresponding dissipation rates (mechanical and thermal) are important information not easily available from experiments. Finally, the power spectra at characteristic monitoring points revealed interesting local dissimilarities between the velocity and temperature fluctuations for selected values of Prandtl number.

Declaration of Competing Interest

None Declared.

CRediT authorship contribution statement

E. Cascioli: Methodology, Software, Validation, Formal analysis, Investigation, Data curation, Visualization, Writing – original draft, Writing – review & editing. **S. Keijers:** Supervision, Writing – original draft. **K. Van Tichelen:** Conceptualization, Supervision, Writing – original draft, Project administration, Funding acquisition. **J.E. Vesper:** Software, Writing – original draft. **S. Kenjereš:** Conceptualization, Methodology, Resources, Visualization, Supervision, Writing – original draft, Writing – review & editing, Project administration, Funding acquisition.

Acknowledgments

We gratefully acknowledge the experimental group of the von Karman Institute for Fluid Dynamics for having provided a unique set of experimental data for the validation of this numerical study. Particularly, our thanks are to Philippe Planquart, Lilla Koloszar, Sophia Buckingham and Agustin Villa Ortiz for their kind professional and personal support. This work was supported by European Commission's H2020-EURATOM program under Grants 654935 (SESAME) and 662186 (MYRTE).

Supplementary material

Supplementary material associated with this article can be found, in the online version, at doi:10.1016/j.ijheatmasstransfer.2022.122774.

References

[1] R. Fernandez, D. De Bruyn, P. Baeten, H.A. Adberrahim, The evolution of the primary system design of the MYRRHA facility, IAEA-CN-245-258 (2017).
[2] K.V. Tichelen, F. Mirelli, M. Greco, G. Viviani, E-SCAPE: A scale facility for liquid-metal, pool-type reactor thermal hydraulic investigations, Nuclear Engineering and Design 290 (2015) 65–77.
[3] S.B. Pope, Turbulent Flows, Cambridge University - Cambridge Univ. Press, 2000.
[4] G. Grötzbach, Challenges in low-prandtl number heat transfer simulation and modelling, Nucl. Eng. Des. 264 (2013) 41–55.
[5] F. Roelofs, A. Shams, I. Otic, M. Böttcher, M. Duponcheel, Y. Bartosiewicz, D. Lakehal, E. Baglietto, S. Lardeau, X. Cheng, Status and perspective of turbulence heat transfer modelling for the industrial application of liquid metal flows, Nuclear Engineering and Design 290 (2015) 99–106.
[6] K. Abe, T. Kondoh, Y. Nagano, A new turbulence model for predicting fluid flow and heat transfer in separating and reattaching flows - II. thermal calculations, International Journal of Heat and Mass Transfer 38 (8) (1995) 1467–1481.
[7] S. Kenjereš, K. Hanjalić, Convective rolls and heat transfer in finite-length Rayleigh–Bénard convection: a two-dimensional numerical study, Physical Review E 62 (6) (2000) 7987.
[8] R.D. Và, S. Manservisi, F. Menghini, A $k-\omega-k_\theta-\omega_\theta$ four parameter logarithmic turbulence model for liquid metals, Nuclear Engineering and Design 101 (2016) 1030–1041.
[9] A. De Santis, A. Shams, Application of an algebraic turbulent heat flux model to a backward facing step flow at low prandtl number, Annuals of Nuclear Energy 117 (2018) 32–44.
[10] A. De Santis, A.V. Ortiz, A. Shams, L. Koloszar, Modelling of a planar impinging jet at unity, moderate and low Prandtl number: Assessment of advanced RANS closures, Annuals of Nuclear Energy 129 (2019) 125–145.
[11] J. Oder, A. Shams, L. Cizelj, I. Tiselj, Direct numerical simulation of low-Prandtl fluid flow over a confined backward facing step, International Journal of Heat and Mass Transfer 142 (2019) 118436.
[12] A.V. Ortiz, L. Koloszar, P. Planquart, Large eddy simulations on a natural convection boundary layer at Pr = 0.71 and 0.025, Nuclear Engineering and Design 353 (2019) 110231.
[13] C.Y. Li, S.V. Garimella, Prandtl-number effects and generalized correlations for confined and submerged jet impingement, International Journal of Heat and Mass Transfer 44 (2001) 3471–3480.
[14] B. Rembold, N.A. Adams, L. Kleiser, Direct numerical simulation of a transitional rectangular jet, International Journal of Heat and Fluid Flow 23 (5) (2002) 547–553.
[15] U. Knebel, L. Krebs, U. Muller, B.P. Axcell, Experimental investigation of a confined heated sodium jet in a co-flow, Journal of Fluid Mechanics 368 (1998) 51–79.
[16] S. Buckingham, Prandtl number effects in abruptly separated flows: LES and experiments on an unconfined backward facing step flow, PhD Dissertation – Université Catholique de Louvain, 2018.
[17] R.I. Issa, A.D. Gosman, A.P. Watkins, The computation of compressible and incompressible recirculating flows by a non-iterative implicit scheme, Journal of Computational Physics 62 (1986) 66–82.
[18] E. Cascioli, S. Buckingham, S. Keijers, K.V. Tichelen, S. Kenjereš, Numerical and experimental analysis of a planar jet with heated co-flow at medium and low Prandtl-number values, Nuclear Engineering and Design 361 (110570) (2020) 1–11.
[19] I.D. Venuta, A. Boghi, M. Angelino, F. Gori, Passive scalar diffusion in three-dimensional turbulent rectangular free jets with numerical evaluation of turbulent Prandtl/Schmidt number, International Communications in Heat and Mass Transfer 95 (2018) 106–115.
[20] N. Kimura, H. Miyakoshi, H. Kamide, Experimental investigation on transfer characteristics of temperature fluctuation from liquid sodium to wall in parallel triple-jet, International Journal of Heat and Mass Transfer 50 (2007) 2024–2036.
[21] A. Fregni, D. Angeli, A. Cimarelli, E. Stalio, Direct numerical simulation of a buoyant triple jet at low-Prandtl number, International Journal of Heat and Mass Transfer 143 (2019) 118466.
[22] M. Germano, U. Piomelli, P. Moin, W.H. Cabot, A dynamic subgrid-scale eddy viscosity model, Physics of Fluids A 3 (1991) 1760–1765.
[23] J. Smagorinsky, General circulation experiments with the primitive equations. i. the basic experiment, Monthly Weather Review 91 (1963) 99–164.
[24] D.K. Lilly, A proposed modification of the Germano subgrid-scale turbulence closure method, Physics of Fluids A 4 (1992) 633–635.
[25] B.W. Righolt, S. Kenjereš, R. Kalter, M.J. Tummers, C.R. Kleijn, Dynamics of an oscillating turbulent jet in a confined cavity, Physics of Fluids **27**, 095107 (2015) 1–16.
[26] B.W. Righolt, S. Kenjereš, R. Kalter, M.J. Tummers, C.R. Kleijn, Electromagnetic control of an oscillating turbulent jet in a confined cavity, Int. J. Heat and Fluid Flow 62 (2016) 395–406**.** Part B
[27] S. Kuhn, S. Kenjereš, P.R. von Rohr, Large-eddy simulations of wall heat transfer and coherent structures in mixed convection over a wavy wall, Int. J. Therm. Sci. 49 (2009) 1209–1226.
[28] C. Wagner, S. Kenjereš, P.R. von Rohr, Dynamic large eddy simulation of momentum and wall heat transfer in forced convection over wavy surfaces, Journal of Turbulence 12 (7) (2010) 1–27.
[29] P. Moin, K. Squires, W. Cabot, S. Lee, A dynamic subgridscale model for compressible turbulence and scalar transport, Physics of Fluids 3 (1991) 2746.
[30] D. Morar, Subgrid-scale heat flux modeling for large eddy simulation of turbulent mixed convection, PhD Dissertation – Karlsruhe Institute of Technology, 2014.
[31] J.E. Vesper, Large Eddy Simulation of Heat Transfer Processes in Energy Systems based on Thermodynamically Consistent Models, MSc Dissertation – Darmstadt University of Technology, 2017.
[32] H.K. Versteeg, W. Malalasekera, An introduction to computational fluid dynamics - The finite volume method, Longman Scientific & Technical, 1995.
[33] A. Smirnov, S. Shi, I. Celik, Random flow generation technique for large eddy simulations and particle dynamics modeling, Journal of Fluids Engineering 123 (2001) 359–371.
[34] S.K. Robinson, Coherent motions in the turbulent boundary layer, Annual Review of Fluid Mechanics 23 (1991) 601–639.
[35] U. Piomelli, E. Balaras, Wall-layer models for large-eddy simulations, Annual Review of Fluid Mechanics 34 (2002) 349–374.
[36] R.W. Davis, E.F. Moore, A numerical study of vortex shedding from rectangles, Journal of Fluid Mechanics 116 (1982) 475–506.
[37] D.J. Price, Modelling discontinuities and Kelvin-Helmholtz instabilities in SPH, Journal of Computational Physics 227 (2008) 10040–10057.
[38] G. Ruiz-Chavarria, C. Baudet, S. Ciliberto, Scaling laws and dissipation scale of a passive scalar in fully developed turbulence, Physica D 99 (1996)**.** 396–380
[39] R.D. Moser, J. Kim, N.N. Mansour, Direct numerical simulation of turbulent channel flow up to $Re_\tau = 590$, Physics of fluids 11 (4) (1999) 943–945.
[40] G.K. Batchelor, Small-scale variation of convected quantities like temperature in turbulent fluid part 1. general discussion and the case of small conductivity, Journal of Fluid Mechanics 5 (1) (1959) 113–133.